Assessment of leading-edge devices for stall delay on an airfoil with active circulation control

M. Burnazzi & R. Radespiel

CEAS Aeronautical Journal
An Official Journal of the Council of European Aerospace Societies

ISSN 1869-5582
Volume 5
Number 4

CEAS Aeronaut J (2014) 5:359-385
DOI 10.1007/s13272-014-0112-5

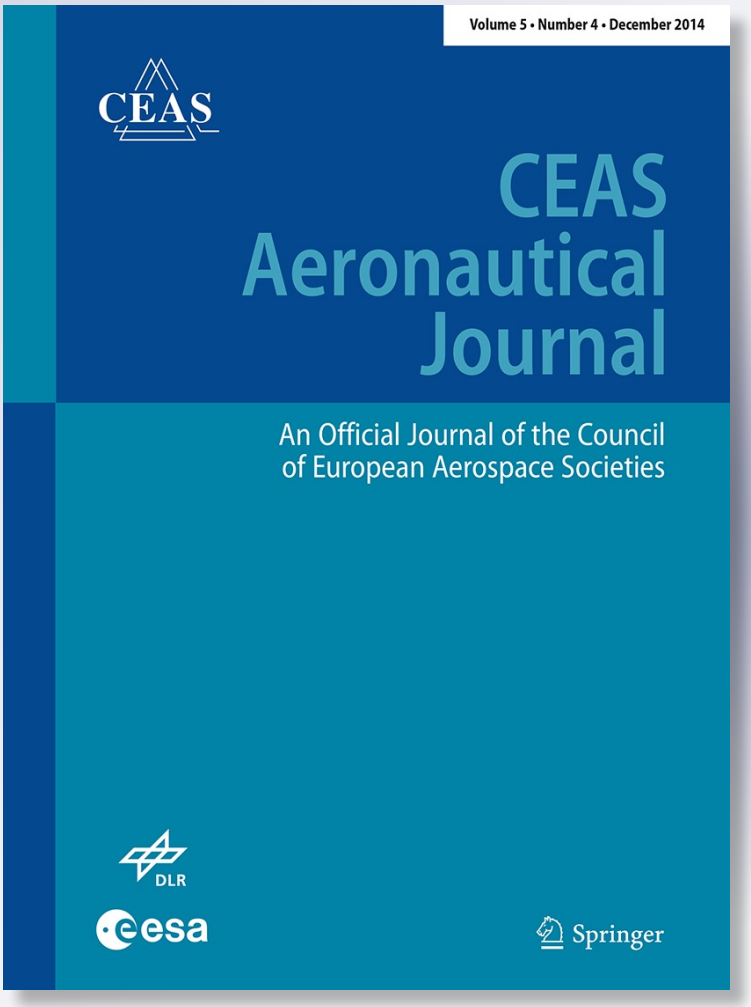

Springer

CEAS Aeronaut J (2014) 5:359–385
DOI 10.1007/s13272-014-0112-5

ORIGINAL PAPER

Assessment of leading-edge devices for stall delay on an airfoil with active circulation control

M. Burnazzi · R. Radespiel

Received: 17 July 2013 / Revised: 28 April 2014 / Accepted: 28 April 2014 / Published online: 27 May 2014

Abstract The use of active, internally blown high-lift flaps causes the reduction of the stall angle of attack, because of the strong suction peak generated at the leading-edge. This problem is usually addressed by employing movable leading-edge devices, which improve the pressure distribution, increase the stall angle of attack, and also enhance the maximum lift coefficient. Classical leading-edge devices are the hinged droop nose or the more effective slat with a gap. The flow distortions generated by the gap become an important source of noise during approach and landing phases. Based on these considerations, the present work aims at evaluating the potentials of gap-less droop nose devices designed for improving the aerodynamics of airfoils with active high lift. Both conventional leading-edge flaps and flexible droop noses are investigated. Flexible droop nose configurations are obtained by smoothly morphing the baseline leading-edge shape. Increasing the stall angle of attack and reducing the power required by the active high-lift system are the main objectives. The sensitivities of the investigated geometries are described, as well as the physical phenomena that rule the aerodynamic performance. The most promising droop nose configurations are compared with a conventional slat device as well as with the clean leading-edge. The response of the different configurations to different blowing rates and angles of attack are compared and the stalling mechanisms are analyzed.

M. Burnazzi (✉) · R. Radespiel
Institut für Strömungsmechanik, Technische Universität Braunschweig, Hermann-Blenk-Str. 37, 38108 Brunswick, Germany
e-mail: m.burnazzi@tu-bs.de

R. Radespiel
e-mail: r.radespiel@tu-braunschweig.de

Keywords High-lift · Flow control · Coanda flap · Droop nose

1 Introduction

The ability of transport aircraft wings to obtain high lift coefficients during take-off and landing is important to allow optimal sizing of the wing for cruise performance. The technology of conventional high-lift systems for this purpose is now well established, in terms of lift-coefficient potentials, mechanical complexity and weight. Maximum lift coefficients achieved for a conventional three-element slotted wing section in its landing configuration are now well above four [1]. This yields an overall aircraft lift coefficients of 2.6–2.8 for a typical swept wing, which is about twice the value of the corresponding clean configuration. Future commercial aviation requirements call for improving the airport community noise, for making point-to-point connections more available, and for reducing aircraft fuel consumption and operating cost. It is expected that these requirements will strengthen the role that the segment of smaller, regional aircraft plays in commercial aviation. In particular, these aircraft should combine cruise efficiency with short take-off and landing capabilities, in order to allow operation at regional airports with all noise sources from engine and airframe kept at the lowest possible level. Preliminary design of cruise efficient aircraft shows that substantial reductions of runway length are only possible by increasing the maximum lift coefficient by significant factors accompanied by a moderate increase of the installed engine thrust [2, 3].

Our research hypothesis for obtaining drastic lift increase at take-off and landing assumes that this can be accomplished using active high-lift systems, where the lift

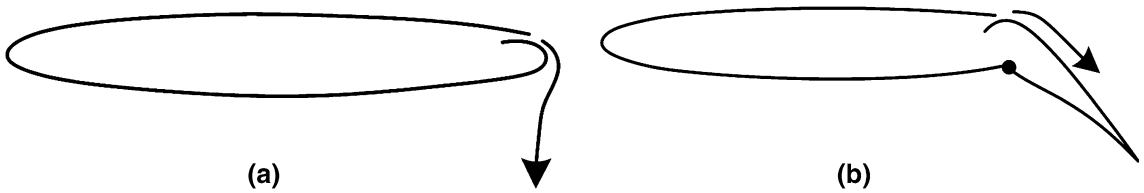

Fig. 1 Internal blowing strategies to obtain high lift coefficients. **a** Coanda circulation control. **b** Internally blown flap

is augmented by a well-designed blowing system. Active circulation control may also provide the required lift coefficients without employing gaps, which are identified as major source of airframe noise during approach and landing [4]. Along this line of thought there is already significant knowledge available that comes from about 80 years of research in active high lift [5, 6].

One class of augmented lift systems is characterized by external blowing, where the propulsive jet of the aircraft engine is used to achieve the lift increase. The relevant physical effects may be described as "vectored slip stream", "externally blown flaps", or "upper surface blowing". These effects yield medium powered lift augmentation for a given thrust-to-weight ratio [7]. Much higher powered lift, on the other hand, is possible using internally blown flaps or by blowing internally supplied air over suited Coanda surfaces close to the trailing-edge, as sketched in Fig. 1.

Both concepts of Fig. 1 use the turbulent flow entrainment of a tangentially blown wall jet to keep the flow attached along the strong turning rate of the specially-designed wall geometry. However, the blunt trailing-edge configuration requires continuous blowing even during cruise in order to keep cruise drag low. This restriction favors a retractable trailing-edge, such as the one shown in Fig. 1b, to create the suited Coanda surface at take-off and landing, hence the term Coanda flap. This second solution may be accomplished by an internally blown flap, and hence, this configuration may also be viewed as a special case of circulation control. In the following sections, the terms "Coanda flap" and "active high-lift flap" are used interchangeably to refer to this configuration. A good overview of the state of the art in the field of circulation control by internal blowing is found in reference [8].

Gad El Hak categorized the various flow control approaches based on their required energy expenditure [9]. He recognized direct tangential injection of momentum into the boundary layer—wall jet—as one of the most effective and feasible flow separation control techniques. Several applications of this principle are discussed by Englar in [10]. This approach has been the interest of several research programs, including the present one. Milholen et al. [11] published experimental results from the NASA-LaRC National Transonic Facility, where high Reynolds number tests were conducted on the "FAST-MAC" model, a tapered, swept and twisted supercritical wing model, equipped with an active circulation control flap. A wall jet was blown tangentially on the suction side of the 15 % chord simple-hinged flap, deflected by 60° in landing configuration.

Computational Fluid Dynamics is an extremely powerful tool for the design of high-lift devices. However, active control represents a challenge for the accuracy of numerical solutions. Allan et al. [12] and Paschal et al. [13] performed 2D numerical and experimental analyses on a circulation control airfoil characterized by a very large circular trailing-edge over which a wall jet was blown. The wide blunt trailing-edge not only makes accurate pressure measurements possible by means of static pressure probes but also represents a large Coanda surface where the accuracy of the numerical approach can be tested for different blowing rates. In fact, in the absence of a separation point fixed by a sharp edge, the Kutta condition depends entirely on the jet trajectory, even for high jet velocity rates. In this case, the solution of a numerical simulation is particularly sensitive to the capability of the turbulence model to accurately estimate the eddy viscosity, also in presence of high flow curvature.

An experimental evaluation of the noise produced by a Coanda flap is documented in reference [14]. A 0.3 m chord airfoil model was equipped with a 30 % chord simple-hinged flap, deflected by 40°. Active circulation control was implemented by a wall jet tangentially blown on the suction side of the flap. The tested configuration and the freestream conditions were very similar to those in the present study. Compared to a three-element high-lift configuration at the same lift coefficient, the gap-less pneumatic high-lift device yields a noise reduction of 5–8 dB in the frequency range from 0.2–2.0 kHz. Note that the relative noise emission of the pneumatic high-lift system appears to be affected by flight speed and blowing rate, as well as angle of attack.

A major requirement for aircraft applications calls for low blowing power of the active control system, to avoid the need for a larger engine. Experiments with variable slot heights [15] revealed that narrow slots lead to higher blowing efficiency, which can be non-dimensionally quantified (Poisson-Quinton and Lepage [16]) by the momentum coefficient.

$$C_\mu = \frac{v_j \dot{m}_j}{\frac{1}{2}\rho_\infty v_\infty^2 S_{\text{ref}}}$$

where v_j and $\dot{m}_j$ are the velocity and the mass flow of the jet at the exit, and S_{ref} is a reference surface, which in the present study is the airfoil chord multiplied by a unit span. Acceptable values of C_μ are determined by the engine design, as the engine represents one of the solutions to provide compressed air to the active high-lift system. Recent studies of the Collaborative Research Center on high lift in Braunschweig use the overall design software PrADO to analyze the effects of active high-lift flaps on aircraft performance [2, 3]. Engine size is usually determined at take-off conditions for the one-engine-out case. The software PrADO then determines the optimal flap deflection angles and the corresponding blowing rates for this case. Table 1 displays unpublished results of these studies with respect to typical engine growth of an advanced turboprop application. Growth of engine weight for bleed air solutions is significant, in the range of 17 %. This is caused by the fact that the bleed air is taken from the low-pressure compressor of the core engine, and as a result, a mismatch in the engine cycle occurs. Generation of compressed air by electrically driven compressors located in the wing yields a better balanced engine cycle and hence the core engine growth is rather small. However, this causes additional mass of the electric generator and the distributed compressor systems. It turns out that the total weight increase needed for supplying compressed air to the local Coanda jet plena from the engine is 37 % of one engine weight, while this number is 40 % for the electrical system.

The efficiency of active blowing can be characterized by the "lift gain factor", defined as the ratio between the lift coefficient increase due to the active circulation control system and the jet momentum coefficient needed to obtain this gain. Recently, reference [17] reviewed the status of published lift gain factors. Thomas [18] determined a lift gain factor of 10 at $Re = 0.8 \times 10^6$. The reason of this limited efficiency was mainly due to the large slot height employed. Additional lift gain factors, referring to leading-edge blowing, were later reported by Gersten and Löhr [19]. However, the gain factor achieved with this type of leading-edge stall protection was even lower. Other results by Englar [20] for a blown 23 % high-lift flap indicated larger possible gains. The lift gain factor was also employed by Poisson-Quinton and Lepage [16] to describe the reduction of efficiency that characterizes the supercirculation regime ($C_\mu > 0.05$ in their case). In the last decades, significant research effort was focused on pulsed blowing, in order to reduce the jet momentum required to avoid separation [6]. In reference [17], it was found that the detailed design of blowing slot height, flap angle and Coanda contour along with the blowing rate has a significant impact on the gain factor. Improvements in gain factor could be obtained using numerical sensitivity investigations to guide the design. Also, extrapolations to flight Reynolds numbers were obtained by numerical flow simulations at low cost relative to experiments. Recent design data [21] reveal that lift gain factors of $\sim$60 were obtained for active airfoils with maximum lift coefficients of $\sim$4 with steady blowing. However, the gain factor decreased rapidly with higher lift coefficients. In addition, significant reductions in maximum lift angles of attack at high flap angles and high blowing rates (at $C_l \approx 6$) were observed. These losses were related to the suction peak at the airfoil nose that is generated by the active high-lift. This calls for aerodynamic means to reduce the losses associated with the flow around the leading-edge. The classical means for this purpose are the droop nose and the slat, as displayed on Fig. 2.

Table 1 Effect of active high-lift systems on overall design of a $M = 0.74$ reference aircraft, for one-engine-out conditions with $C_\mu \approx 0.025$

Configuration	Take-off length, in (m)	Passengers	Engine mass + pipes, electric compressors, generators, in (Kg)
Turboprop, conventional high-lift [2]	1,100	100	1,256 + 0
Turboprop, Coanda flap: bleed air [2]	800	100	1,467 + 259
Turboprop, Coanda flap: electric compressors	800	100	1,283 + 472

The motivation behind a droop nose leading-edge device is to reduce the suction peak at the nose, while a second suction peak is generated around the hinge line of the device. Significant experience exists in how much stall protection mechanisms extend the maximum lift coefficient and the angle-of-attack range for applications with conventional high-lift flaps such as Fowler flaps. Quantitative numbers depend on the clean airfoil geometry and geometrical design constraints. However, a qualitative idea is obtained by examining the results of the DLR high-lift research program (Wild [1]), where a transonic wing section with a single-slotted Fowler flap and different leading-edge devices were examined. The results are summarized in Table 2.

The values reported in the table correspond to Mach number 0.2 and Reynolds number 5×10^6. Reference [1] focuses on the Mach number and Reynolds number effects on the performance of the various high-lift configurations displayed in Table 2. The paper discusses the compressibility effects generated by the high speed at the leading-

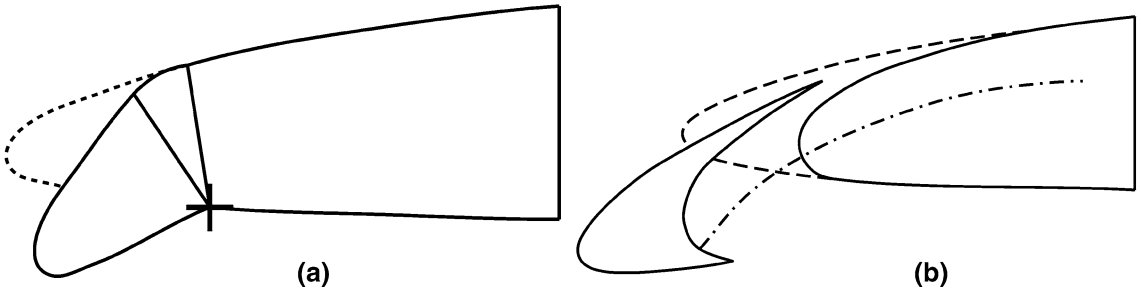

Fig. 2 Conventional approaches for stall protection through leading-edge devices. **a** Droop nose. **b** Slat

Table 2 Enhancement of high-lift behavior of DLR F15 airfoil using leading-edge devices at $M = 0.2$ and $Re = 5 \times 10^6$, according to [1]

	$C_{l,\ max}$	α_{stall} (°)
Fowler flap alone	3.2	8.5
		
Fowler flap and slat	4.6	31.0
		
Fowler flap and morphing droop nose	3.6	14.0
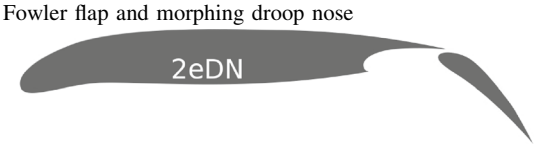		

edge. The blowing slot of an active high-lift device represents another area that is particularly prone to compressibility effects. Reference [11] describes the effects of high local Mach number at the blowing slot exit, where it was shown that for a freestream Mach number of 0.2 sonic condition at the nozzle exit causes the jet to separate from the flap. This problem is circumvented for a lower Mach number of $M = 0.1$. The current investigations are conducted at $M = 0.15$, where no separation as a result of compressibility effects was observed. The physical characteristics of the flow at the slot exit section at different blowing rates are discussed in Sect. 4.

Published knowledge on leading-edge stall protection for active high-lift flaps is rare. Previous studies showed the potential of extending flow control to the leading-edge, in order to avoid separation [10, 21–25]. However, even though these attempts succeeded in delaying stall, the lift gain factor was significantly reduced by the considerably high jet momentum required at the leading-edge. Leading-edge blowing as stall protection is discussed in more detail in Sect. 2.2.

It has to be concluded from these studies that the full benefit of using active high-lift flaps can only be exploited if the leading-edge becomes part of the design space and the sensitivities of the leading-edge flow are better understood. This is the field of research addressed by the present work. The objective of the present paper was to contribute to the understanding of how high lift coefficients are obtained at low mechanical power consumption, and how they depend on the leading-edge flow. The following design guidelines form the basis of the current research:

- The high-lift device at the trailing-edge employs active circulation control using tangential blowing on a simple-hinged flap. This concept enables large lift gains and it can be adapted to meet different operative requirements by varying flap deflection and blowing rate. Using movables at the trailing-edge allows for clean cruise geometry without any drag penalties.
- The aerodynamic design strives for gap-less high-lift devices. Both the trailing-edge and the leading-edge devices should avoid gaps, because the flow across gap edges is a major source of airframe noise generation [6].

The present paper presents significant improvements on the airfoil shape to obtain high lift gain factors. The research work is performed within the framework of the Collaborative Research Centre, SFB 880: “Fundamentals

of High Lift for Future Civil Aircraft" at TU Braunschweig, Germany. Section 2 briefly describes the status of Coanda flap design using a fixed geometry of the leading-edge and wingbox. It was shown that very high circulation due to the trailing-edge device requires an effective leading-edge stall protection, in order to avoid those local losses from the leading-edge dominating the flow behavior. Following the guideline to avoid gaps, some fixed percentage of the chord length (that is the part of the airfoil not needed for the wing box) is then modified in order to obtain a droop nose configuration. The new leading-edge shape brings about continuous changes to the original camber and thickness distributions.

Previous studies, conducted by Kühn and Wild, focused on the combination of a flexible droop nose and a fowler flap [26]. Shmilovich and Yadlin compared a rigid droop nose device that rotated around a hinge line and a conventional slat in combination with an active high-lift flap with boundary-layer control [27]. Their slat configuration yielded a higher stall angle, compared to the droop nose. They also discussed the complexity of flow interactions generated by a slotted device [28]. For instance the viscous slat wake exhibited a sudden spreading as it was exposed to a strong adverse pressure gradient along the flap. Such interactions can limit maximum lift, even without boundary layer separation from the airfoil surface [29]. An optimization approach for a droop nose bending around a hinge line and a comparison of the resulting geometry with a Krueger flap are presented by Jirásek and Amoignon [30]. The present paper extends the existing knowledge on the flow physics of suited leading-edge devices for applications with rather high lift coefficients, as obtained with Coanda flaps.

The methods and design steps that led to the aerodynamically most effective leading-edge shape are briefly described in Sect. 5. More details about the shape design and the effects of different geometrical parameters on the aerodynamic performance can be found in [31]. The resulting shape-morphing droop nose shows significant improvements of the blowing efficiency and hence its suitability for application in civil transport aircraft. The flexible droop nose geometry is then compared to a rigid leading-edge flap, a conventional slat configuration and the baseline geometry (without leading-edge device). Comparisons at constant blowing rate and at constant angle of attack are presented in Sect. 6, in order to describe the effects of these two important parameters on the flow dynamics generated by the different leading-edge configurations. In Sect. 6 also the maximum lift behavior and gains for variations of blowing rate are addressed. The analyses discussed in the present paper yield physical insight into the viscous losses in active high-lift systems and into particular stalling mechanisms not known before.

2 Previous results

2.1 Design of the Coanda flap

This section describes previous numerical and experimental work aimed at improving the lift gain factor by careful design adjustments of the trailing-edge device while keeping the leading-edge geometry fixed. These initial design studies assumed steady blowing to produce suited turbulent wall jets that exploit the Coanda effect for effective flow turning. The free flow conditions employed during these previous analyses were: $Re = 20 \times 10^6$, and $M = 0.15$. The most important design parameters were flap deflection angle, the momentum coefficient of blowing and the blowing slot height [24]. While flap angle and blowing momentum coefficient should increase for increased lift targets, optimal slot heights were rather small, with values of around 0.0006 times the airfoil chord length. Surprisingly, the optimum slot height was independent of the flap angle. Figure 3 displays a typical design result, where the transonic airfoil DLR F15 is equipped with an internally blown flap set at 65° deflection angle. The detailed curvature distribution of the Coanda surface used as flap knuckle shape was found less important. Values of the radius of curvature of around 0.07 times the chord length are a reasonable design choice. Also the flap length suited to achieve high lift gains could be identified. Best lift gain factors were obtained with flap lengths of 0.25–0.30 times the airfoil chord [21].

With these design choices typical lift gains over blowing momentum (lift gain factor) of 66 were obtained at a lift coefficient around 4 and with a flap deflection angle of 50°, whereas this value was reduced to 48 at a lift coefficient around 6 and flap deflection of 80°. For each flap setting, different blowing rates were tested in order to identify the minimum value that provides attached flow on the flap, which yields the maximum lift gain factor. For 50° and 80° flap deflections, the optimal jet momentum coefficients are 0.025 and 0.078, respectively. The corresponding ratio between jet velocity (averaged along the slot exit section) and freestream velocity is $\sim$4.4 for $C_\mu = 0.025$ and $\sim$6 for $C_\mu = 0.078$.

These design studies were accompanied by significant efforts to validate the numerical simulations performed with the RANS solver. Simulations of Coanda wall jets over a blunt trailing-edge showed the necessity to augment standard turbulence models with correction terms to take into account streamline curvature effects on turbulent transport (see reference [32]) similarly as found by Swanson and Rumsey [33]. Airfoil wind tunnel experiments were performed to verify the Coanda flap design and the results were compared to 3-D flow simulations that included the wind tunnel wall effects [34, 35]. These

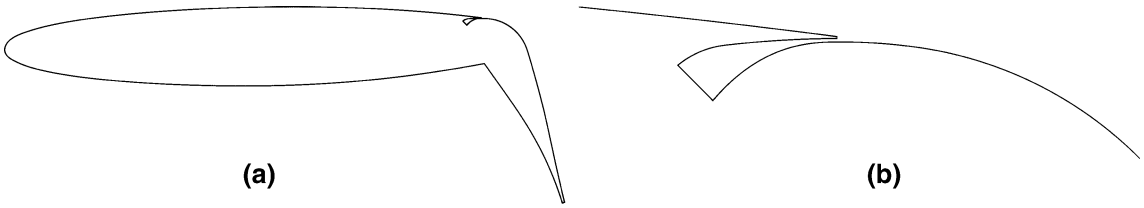

Fig. 3 DLR F15 airfoil equipped with a high-lift flap with internal blowing using a suited Coanda geometry: baseline of the present work. **a** Complete airfoil. **b** Detail of the blowing slot

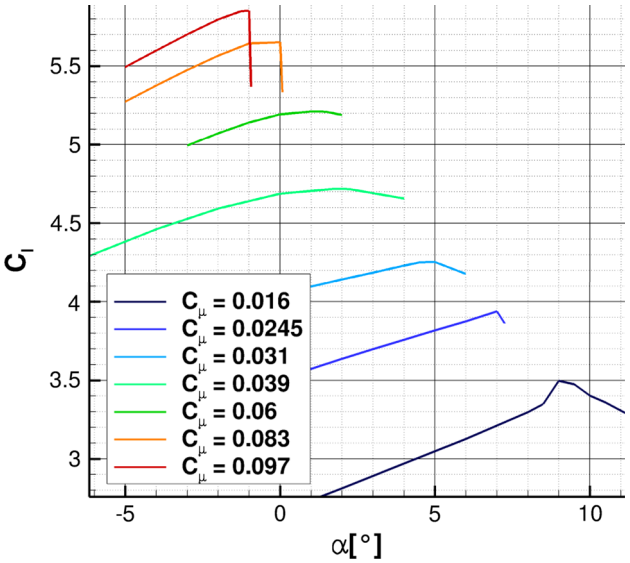

Fig. 4 Effect of blowing momentum on the angle of maximum lift for the DLR F15 airfoil with 65° flap angle, computed for $M = 0.15$, $Re = 12 \times 10^6$

studies revealed good agreement in terms of maximum lift and the corresponding angle of attack, as detailed in Sect. 3.

It was generally noticed though that the angle of attack of maximum lift reduces significantly at higher blowing rates, as seen in Fig. 4 for a typical wind tunnel Reynolds number.

As the adverse pressure gradient along the suction side, downstream of the suction peak at the nose, grows rapidly with the angle of attack it creates significant momentum losses towards the trailing-edge device. This adversely affects the ability of the wall jet to provide flow turning. Local blowing at the nose or at other locations of the airfoil did not help much, as it extended the useful angle-of-attack range but generally at the cost of decreasing the lift gain factor, as described in the next section.

2.2 Leading-edge blowing

A first attempt to improve the stall angle of attack was blowing from a slot at the leading-edge. These studies, documented in reference [24], were conducted with the same airfoil employed in the present work. The analysis was first performed with a 30 % chord Coanda flap, deflected by 80°, at freestream Mach number 0.125 and $Re = 18 \times 10^6$. In this condition, the optimal blowing rate is 0.083, which is the minimum to avoid flow separation from the flap. Stall appeared at −4° because of leading-edge separation, resulting in a lift gain factor of 42. In order to avoid separation, a blowing slot was placed at about 0.02 % of the airfoil chord, downstream of the suction peak. Leading-edge blowing with $C_\mu = 0.043$ yielded an increase of $C_{l,max}$ of 0.45, decreasing the lift gain factor to 33, because of the augmented overall C_μ. However, distributing in this way $C_\mu = 0.126$ between the two blowing locations resulted in higher lift than employing the whole blowing momentum at the flap device. Figure 5a summarizes these results. Further analyses were performed deflecting the Coanda flap by 60° and with $M = 0.15$. In this case, the optimal blowing rate was 0.05 and stall occurred without leading-edge separation: a separation bubble appeared at the leading-edge only 3° after the incidence of maximum lift. Now, the increase of circulation due to leading-edge blowing ($C_\mu = 0.033$) induced supersonic flow at the point of maximum speed around the nose, as shown in Fig. 5b. This made blowing from the two slots less effective than employing the same overall blowing momentum only at the flap. To summarize, these studies revealed that only for high blowing rates, which are justified by high flap deflection angles, leading-edge blowing is effective to delay stall and increase the maximum lift coefficient. However, also in these cases, the efficiency of the high-lift system, expressed by the lift gain factor, decreases with leading-edge blowing.

A similar configuration was tested also by Englar [22]. In this case, a leading-edge blowing slot, positioned at 0.5 % of the airfoil chord, was combined with a trailing-edge 10 %-chord simple-hinged flap, deflected by 90°. The optimal leading-edge blowing rate was obtained for $C_\mu = 0.1$, while the C_μ at the flap was varied from 0.0 to 0.28. The performance of the leading-edge active flow control was compared to a Krueger flap deflected by 60°. The leading-edge blowing was found more effective than the mechanical device at zero or low flap blowing rates:

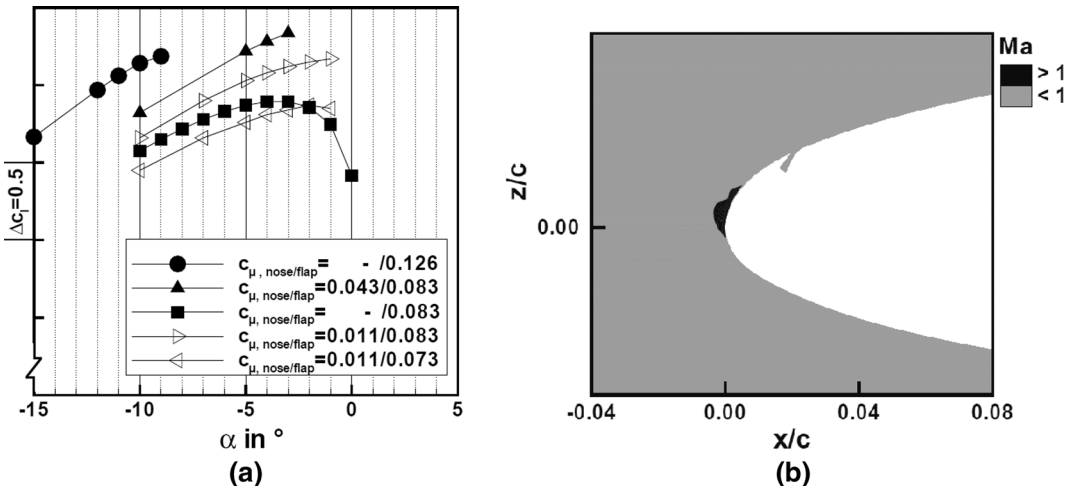

Fig. 5 Leading-edge blowing on DLR F15 airfoil with Coanda flap, from reference [24]. **a** C_l over α for leading-edge blowing: $M = 0.125$, $Re = 18 \times 10^6$, flap deflection 80°, from [24]. **b** Transonic flow at the leading-edge: $M = 0.15$, $Re = 18 \times 10^6$, flap deflection 60°, $\alpha = 7°$, $C_{\mu,\text{nose/flap}} = 0.033/0.050$, from [24]

until $C_\mu = 0.075$ the active LE control yields to 4°–5° higher stall angle of attack with respect to the Krueger flap. For higher flap blowing momentum, however, the pneumatic leading-edge appeared less effective with lower maximum lift coefficient compared to the Krueger flap.

The aerodynamic design work and analyses presented in the following sections describe a suitable aerodynamic solution to improve the stall angle of attack without increasing the overall blowing rate.

3 Numerical set-up

The present investigations are based on 2D simulations of the DLR F15 airfoil with different nose shapes. The CFD solver employed to perform the analysis is the DLR TAU-Code [36, 37]. The Reynolds Averaged Navier-Stokes (RANS) equations are solved using a finite volume approach. The employed discretization schemes are the central scheme and the second-order upwind Roe scheme for the mean-flow inviscid flux and the convective flux of the turbulence transport equation, respectively. The turbulence model is that of Spalart and Allmaras with curvature correction (SARC) [38]. This extension allows the one-equation turbulence model to maintain a good accuracy in regions where the streamlines have a high curvature. This characteristic is fundamental for the simulation of the Coanda phenomenon, which is based on the equilibrium between the inertial forces and the momentum transport in the direction normal to the convex surface, reference [32].

Freestream Mach number 0.15 may represent a challenge for compressible solvers such as TAU. The challenge arises from the large disparity of the acoustic wave speed and the waves convected at fluid speed, which increases the stiffness of the equation system. One typical approach to solve this issue and improve convergence and accuracy is to use preconditioning. Unfortunately, for the present simulations preconditioning did not succeed, and fluctuations that slowed down convergence and prevented a steady solution from being established were observed. The authors believe that the very large range of Mach numbers present in the flow field is the reason behind the preconditioning failure. However, these fluctuations caused by preconditioning disappeared when an unsteady time integration approach was used. This suggests that preconditioning makes the numerical solution more sensitive to local flow unsteadiness, e.g., at the blunt trailing-edges of the flap and of the lip above the blowing slot. It is worthwhile to note that the solution obtained by unsteady time integration and preconditioning did not show any significant difference from the steady approach without preconditioning. Hence, all results presented in the subsequent sections are for numerical results without preconditioning.

The numerical scheme and the turbulence model have been previously assessed by comparing the results to wind tunnel experiments [34, 35]. Figure 6 shows one typical comparison between experimental and numerical results [34]. The shown numerical simulation was conducted for the same airfoil and flap configuration as employed in the present paper (albeit with a different flap angle), using the same solver and the same numerical approach as in the present work. It was noted that good agreement with the wind tunnel results could be only obtained from 3D simulations that include the side-wall boundary layer. At low blowing rates, when separation occurred over the flap, the curvature correction module of the turbulence model appeared to be necessary in order to better predict the flow separation point on the flap. The velocity profiles extracted

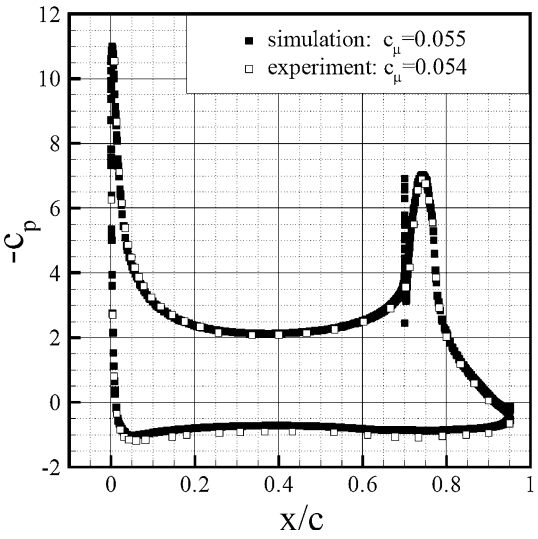

Fig. 6 Comparison of C_p distributions from numerical simulations and wind tunnel experiments [34], $M = 0.15$, $Re = 1 \times 10^6$, $\alpha = 0°$, flap deflection 45°, $C_\mu = 0.055$

from about 3 % of the chord upstream of the blowing slot showed a maximum discrepancy of 5 % between the numerical and experimental data (not shown here). The flow fields were comparable even in the areas next to the wind tunnel walls, where complex 3D phenomena occurred.

A partially separated flow is inherently unsteady. Therefore, it was not always possible to establish a steady converged solution. This unsteadiness was evident in the lift coefficient, where constant amplitude fluctuations were observed after an initial transient period. The maximum observed amplitude of these fluctuations was always well below 1 % of the average lift coefficient. All aerodynamic coefficients discussed in the present paper represent the average of these slightly oscillating data.

Convergence was assumed when the lift coefficient (averaged in case of fluctuations) variation dropped below 1×10^{-6} during the last 500 iterations. Under this constraint, density residuals are converged by $\sim$5 orders of magnitude with respect to the initial solution. The initial solution was obtained by applying the freestream flow condition to the entire numerical field.

The lift, drag and pitching moment coefficients were determined by integrating the pressure and shear stress distributions over the airfoil surface. Hence, the contribution from the added jet momentum was not included.

Due to the high number of required simulations, the mesh density was determined by means of a mesh convergence exercise based on the Richardson extrapolation [39]. This procedure provides an estimation of the space discretization error and of the minimum number of points that produce acceptable accuracy. Three different grid densities with $\sim$70,000, 230,000 and 920,000 points were tested. The corresponding maximum lift coefficients of 4.410, 4.456 and 4.480 were obtained for the three grids at $\alpha = 3.0°$. Based on these values, the Richardson extrapolation yielded a maximum lift coefficient of 4.496, which is an approximation of using an infinite large number of grid points. This value was used as a reference lift coefficient to determine the grid resolution error, which was 1.91, 0.89 and 0.36 % for the three grids, respectively. As such, the medium grid, with $\sim$230,000 points was chosen, which represented a compromise between accuracy and computational cost. This analysis was performed using $C_\mu = 0.0356$ because this coefficient turns out to be particularly suited as described in Sect. 6.3.3.

The grid is composed of a structured and an unstructured region. As shown in Fig. 7, the structured grid layer extends from the airfoil surface outward to cover the region where the main viscous phenomena occur. The viscous sub-layer is also resolved, with $y^+ < 1$ everywhere over the airfoil surface. An important characteristic of the grid, that makes it suitable for high-lift simulations, is the grid density along the pressure side, as the stagnation point will be situated in this region, and can move quite far from the leading-edge. Therefore, a high amount of points is necessary to properly capture the flow attachment (Fig. 7b). The structured region is extended over a large area over the flap, in order to accurately capture vortices expected in case of flow separation from the flap. Both the trailing-edge and the edge of the slot lip are discretized by means of a local C-block topology, in order to avoid the propagation of high point density into areas where grid points are not needed, which could slow down the convergence, see Fig. 7c, d).

4 Compressibility effects

Wild, in [1], focuses on the effect of Mach number and Reynolds number on the performance of different high-lift configurations. As shown in Table 2, a trailing-edge Fowler flap was combined with a slat and a flexible droop nose configuration, and their behavior was compared with the baseline configuration, represented by the airfoil without leading-edge device. The study showed that the slat configuration can suffer from a decrease of maximum lift for a freestream Mach number higher than 0.2, which is caused by supercritical flow at the leading-edge of the slat. On the other hand, the droop nose exhibited no decrease in lift due to supercritical flow for Mach numbers up to 0.25.

The second region where compressibility might be critical is the Coanda surface. The wall jet tangentially blown on the suction side of the flap is created by imposing a total pressure inside the plenum at the beginning of a

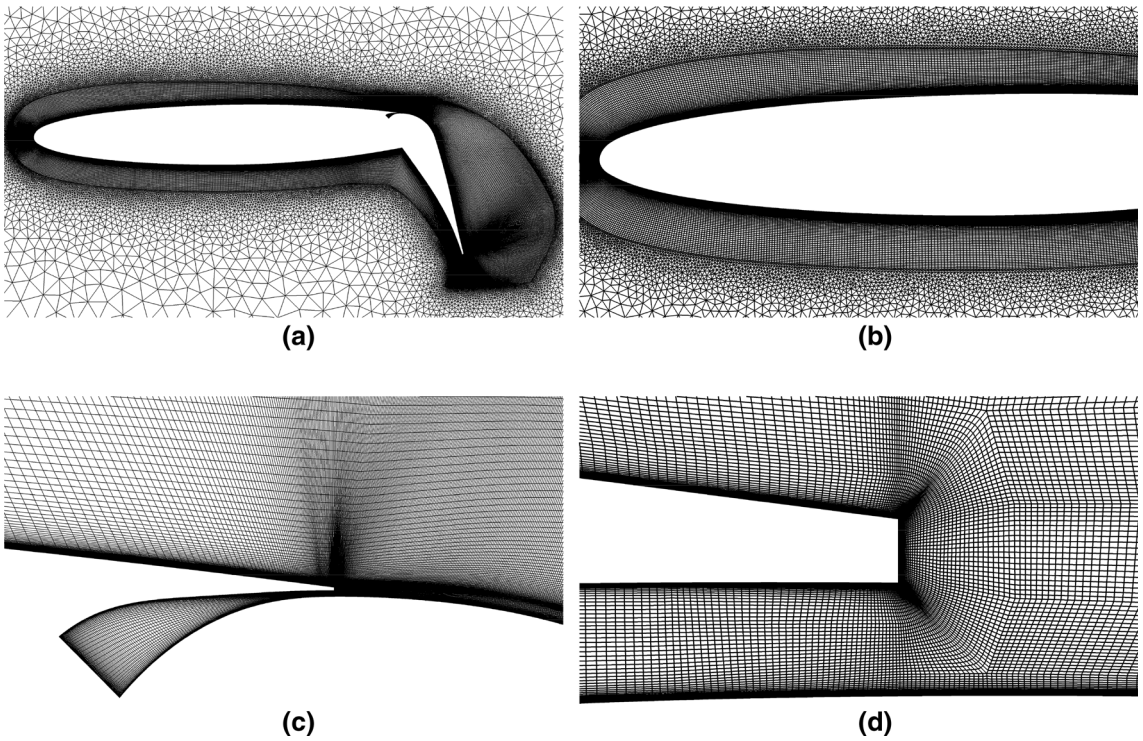

Fig. 7 Numerical hybrid grid used for the analyses. **a** Mesh around the entire airfoil. **b** Points on the main wing. **c** Mesh of plenum and mixing area. **d** C-block topology at the plenum exit section

nozzle (see Fig. 3b). At the exit section, the critical pressure ratio of 0.52828 can be easily reached, causing supersonic expansion of the jet outside of the nozzle. Milholen et al. [11] described this condition and how it affects the performance of the high-lift airfoil. Their research on a half-span aircraft model, equipped with an active high-lift configuration similar to the present one (FAST-MAC model), showed a strong relation between the active high-lift system and compressibility effects for momentum coefficients higher than 0.1 and a freestream Mach number of 0.2. Under these conditions, the jet separates from the flap, causing a significant loss of lift. For a freestream Mach number of 0.1, this separation was not observed, even for supercritical jet conditions.

The freestream Mach number employed in the present paper is 0.15 for all the simulations. At this Mach number, no significant shocks at the leading-edge with adverse effects on maximum lift were observed. Figure 8 shows the variation of jet velocity, density and Mach number for a range of C_μ values. Critical nozzle conditions appear around $C_\mu = 0.052$, when the ratio between the static pressure at the exit section of the nozzle, and the total pressure imposed as boundary condition at the base of the duct reaches 0.5587. For higher blowing rates, the increase in mass flow rate is achieved by increase of density. Figure 9 displays the power ratio in relation to the momentum coefficient. The power ratio is defined as follows:

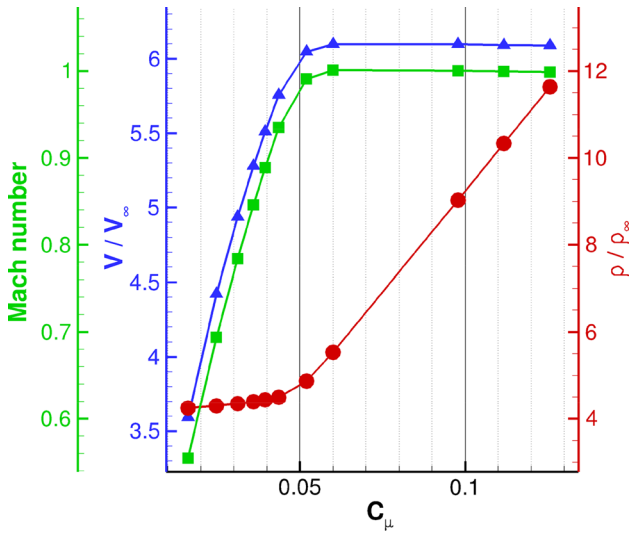

Fig. 8 Jet flow characteristics, $M = 0.15$, $Re = 12 \times 10^6$

$$P_R = \frac{\Delta L_{\max} \cdot v_\infty}{P_j} = \frac{\Delta C_{l,\max} \rho_\infty v_\infty^3 S_{\text{ref}}}{\dot{m}_{\text{jet}} v_{\text{jet}}^2} = \frac{\Delta C_{l,\max} v_\infty}{1/2 C_\mu v_{\text{jet}}}$$

where P_j is the power required to generate the jet, and $\Delta L_{\max}$ is the lift gain referred to the no-blowing condition. The trend slope is progressively reduced by an augmentation of the required power, becoming linear when sonic regime at the nozzle exit occurs.

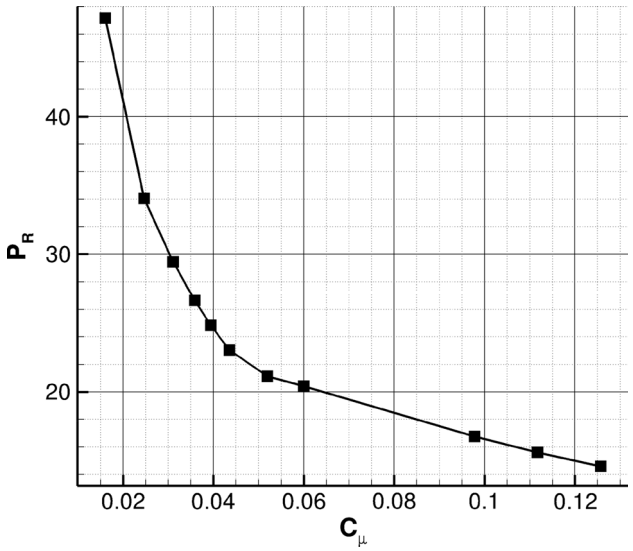

Fig. 9 Power ratio of the Coanda jet per meter span, $M = 0.15$, $Re = 12 \times 10^6$, standard sea-level atmosphere

5 Leading-edge configurations

5.1 Droop nose shapes

For the droop nose, an important requirement based on structural considerations is the skin length of the modified surface which has to remain equal to that of the original airfoil. Studies on the potentials of flexible materials are presented in reference [26], where the benefit of a droop nose combined with a Fowler flap is discussed. In the present work, the search for an effective shape begins with the simple deflection of the fixed nose shape, followed by a symmetrical increase of its thickness and a progressive increase of the mean line camber. Similar parameters were varied by Kühn and Wild [26], where the geometry was obtained through an optimization process. The final droop nose geometry presented by Kühn and Wild [26] exhibited a much lower nose deflection than the current one. This difference is attributed to the different trailing-edge device between the two studies.

In the following, several geometries are evaluated and compared by computing the maximum lift coefficient and the respective angle of attack. At this step of the analysis, Reynolds number, Mach number, blowing momentum, flap deflection angle and flap length are kept constant: $Re = 2 \times 10^7$, $M = 0.15$, $C_\mu = 0.06$, $\delta = 65°$, $L_f/c = 0.25$. With these flow conditions and geometrical settings the velocity ratio between the jet velocity, averaged across the slot exit, and the freestream velocity is 6.1. The droop nose length is fixed to $L_n/c = 0.20$.

5.1.1 *Rigid droop nose*

A first simple leading-edge device is obtained by deflecting the leading-edge downward, without changing its shape (Fig. 10a). Therefore, this technique does not involve structural deformations (except for the hinge-cover sheet at the lower surface) and can be realized by a simple rotation of the nose around a hinge. Thanks to its efficiency and mechanical simplicity, this device is currently employed by some of the current commercial transport aircraft.

This configuration is characterized by two strong peaks of low pressure over the nose, as the deflection of the nose creates a new region of high curvature on the suction side. Nevertheless, the improvement of lift with respect to the baseline configuration is significant, as shown in Fig. 10b, where the deflection is expressed by the angle β. The increase of performance appears to be limited to $\beta = 30°$, as after this value the lift curves present lower maximum lift and a degraded stall angle. Figure 11 displays the friction coefficient for $\alpha = 6°$ and different nose deflections. The results show the progressive load transfer on the boundary layer from the leading-edge to the high curvature region over the hinge with increasing β. Note that with $\beta = 5°$ the airfoil stalls at 4°, so the distribution shown in Fig. 11 represents an already stalled flow. Due to this early stall, it was not possible to include the skin friction distribution for the baseline leading-edge configuration.

The performance decrease after $\beta = 30°$ can be explained by the boundary-layer behavior over the suction side. Figure 12 displays the boundary-layer momentum thickness extracted from the suction side at 22 % of the airfoil chord, just downstream of the hinge location, for $\alpha = 6°$. As the figure shows, until $\beta = 30°$ a deflection of the rigid droop nose reduces the viscous losses within the boundary layer, whereas after this value the momentum thickness increases, indicating higher viscous losses that occur upstream of that location. These losses are caused by the suction peak over the hinge, which becomes stronger with a high wall curvature, as shown in Fig. 13. The performance increase resulting from the nose deflection is also related to the reduction of the transonic area at the leading-edge. For nose deflections lower than $\sim 25°$, the pressure coefficient at the leading-edge is below -25.5, which is the critical value corresponding to sonic flow.

Higher angles of attack decrease the pressure in the front part of the airfoil. Figure 14 displays how the load distribution around the nose changes with the angle of attack. Both suction peaks become larger with higher angles of attack, with the highest increment occurring at the leading-edge. However, even at high angles of attack no separation is observed (Fig. 15). Note that the improvements in lift and angle of attack range are significantly larger than those

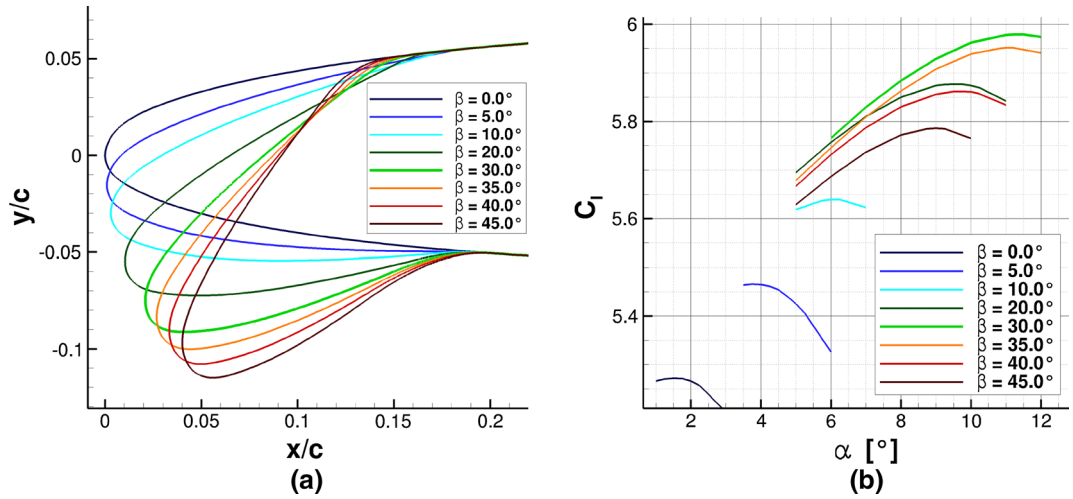

Fig. 10 Shapes and performance of rigid droop nose configurations. **a** The different rigid droop nose shapes. **b** C_l (α) performance for various droop nose shapes, $Re = 2 \times 10^7$, $M = 0.15$, $C_\mu = 0.06$

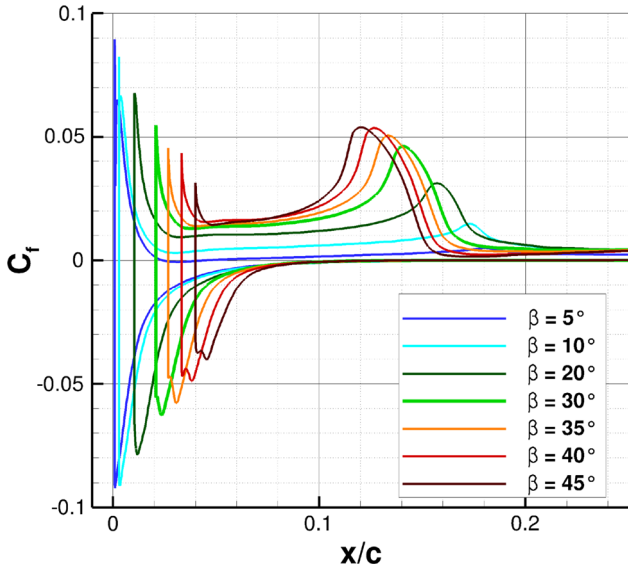

Fig. 11 Skin friction coefficient for different rigid nose deflections, $\alpha = 6°$, $Re = 2 \times 10^7$, $M = 0.15$, $C_\mu = 0.06$

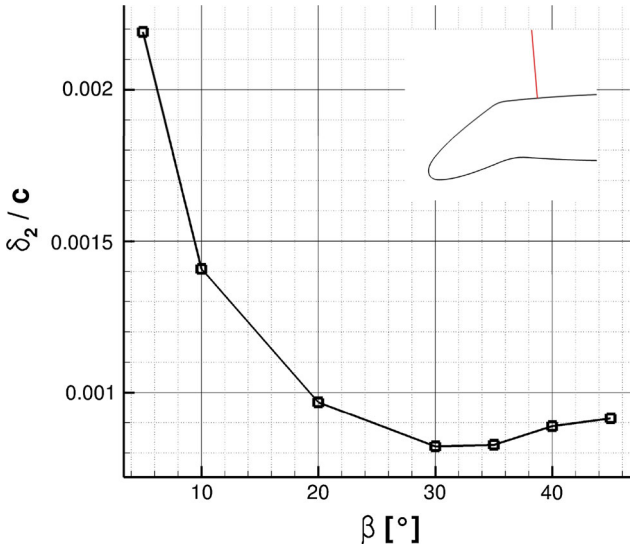

Fig. 12 Boundary-layer momentum thickness on the suction side at 22 % of the airfoil chord, $\alpha = 6°$, $Re = 2 \times 10^7$, $M = 0.15$, $C_\mu = 0.06$

known from applications in combination with mechanical high-lift flaps [40].

5.1.2 *Flexible droop nose*

In order to better control the pressure distribution and avoid large suction peaks on the nose, the shape of the baseline is progressively morphed. The first stage in the flexible design process is a gradual increase of thickness, which decreases the local curvature at both the leading-edge and the hinge knee. The nose geometry is then obtained by multiplying the distance between the contour and the camber line by a parabolic function, which is defined imposing a smooth connection with the wingbox. The resulting thickness variation is symmetric with respect to the camber line and is controlled by a single parameter: the value of the parabolic function at the leading-edge, th_{le}, as shown in Fig. 16a. The highest benefit is obtained for $th_{le} = 1.6$, which delivered a lift coefficient and stall angle increase of 4 and 2.7°, respectively, when applied to a rigid droop nose deflected by $\beta = 10°$ with $C_\mu = 0.06$.

The second stage in the morphed design process gradually increases the camber starting from the baseline configuration, as illustrated in Fig. 16b. This camber increase makes it possible to avoid the high local curvature present over the hinge, which is responsible for degraded

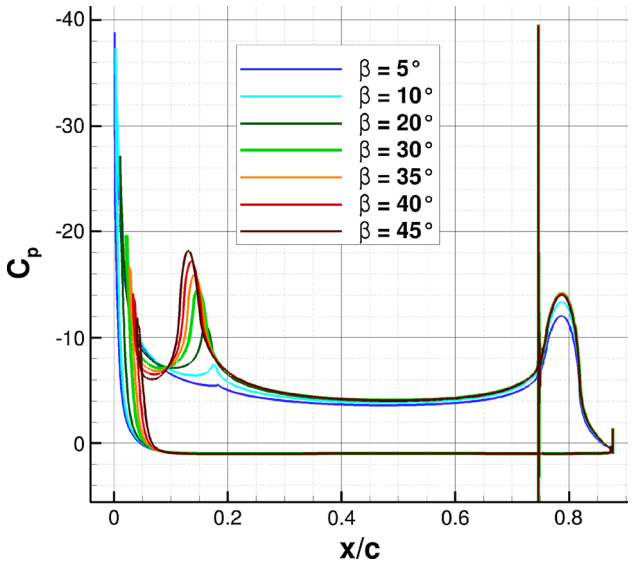

Fig. 13 Pressure coefficient distribution for different rigid nose deflections, $\alpha = 6°$, $Re = 2 \times 10^7$, $M = 0.15$, $C_\mu = 0.06$

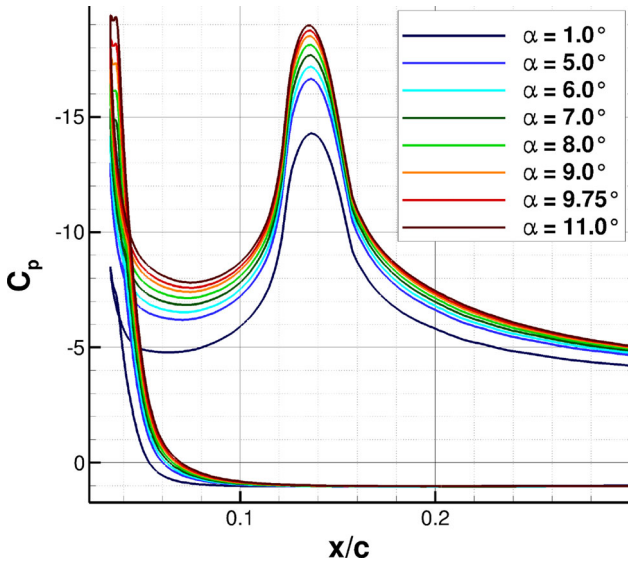

Fig. 14 Variation of pressure coefficient distribution with angle of attack, $\beta = 40°$, $Re = 2 \times 10^7$, $M = 0.15$, $C_\mu = 0.06$

performance at high, rigid nose deflections. The nose deflection is now defined by the angle of the camber line at the leading-edge, γ, which is limited to 90°. Figure 17 shows the trend of maximum lift coefficient for different values of β and γ, which refer to rigid deflection and smooth camber increase, respectively. At low deflections the rigid droop nose appears to be slightly more effective than the flexible one. However, after $\beta = 30°$ the rigid device exhibits poorer performance, as discussed in the previous section, whereas the maximum lift for the flexible droop nose continues increasing and yields a maximum lift at $\gamma = 90°$.

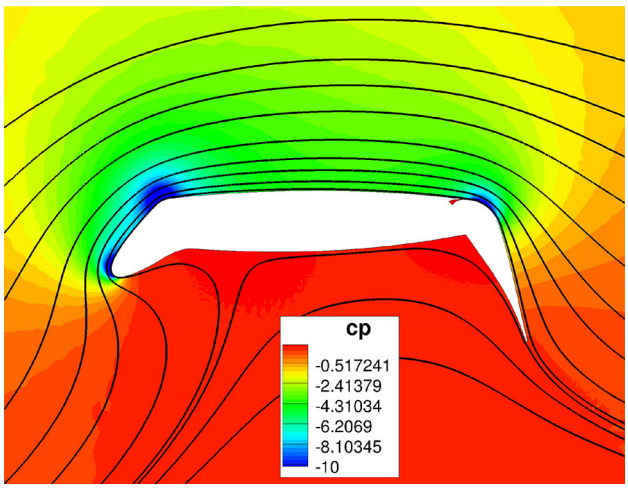

Fig. 15 Pressure coefficient flow field and stream lines in post-stall condition, for $\beta = 40°$, $\alpha = 11.0°$, $Re = 2 \times 10^7$, $M = 0.15$, $C_\mu = 0.06$

For the final stage, both the camber and the thickness are increased, as shown in Fig. 16c. The flexible configuration analyzed in the following sections is defined by $\gamma = 90°$ and $th_{le} = 1.6$, and will be referred to as "flexible droop nose". A more detailed analysis on the separate effects of the progressive cambering and the thickness variation, as well as details about their implementation, is described by Burnazzi [31].

5.2 Slat configuration

The slat configuration, shown in Table 2, was designed by Wild [1]. It is named 3eOpt and has a deflection angle of 28°. It is worthwhile to note that the slat contour was designed for a generic 3D wing in landing configuration equipped with a trailing-edge Fowler flap. Slat angle and gap were determined using numerical optimization of the 2D flow. For the current application with the Coanda flap, the slat performance could most probably be improved by adapting the slat angle and its location to the high circulation generated by the active flap. However, optimizing the slat configuration is not the objective of the present study, and the employed configuration is deemed representative of the flow features and performance trends that an optimized geometry would show, at least for moderate blowing momentum coefficients up to 0.05.

5.3 Effect of the leading-edge configuration on the Coanda flap

As shown in Fig. 18a, the trajectory of the jet is determined by two opposing effects. On one side the jet is kept attached to the flap surface by the Coanda effect. On the other side, the inertia of the outer flow, which comes from

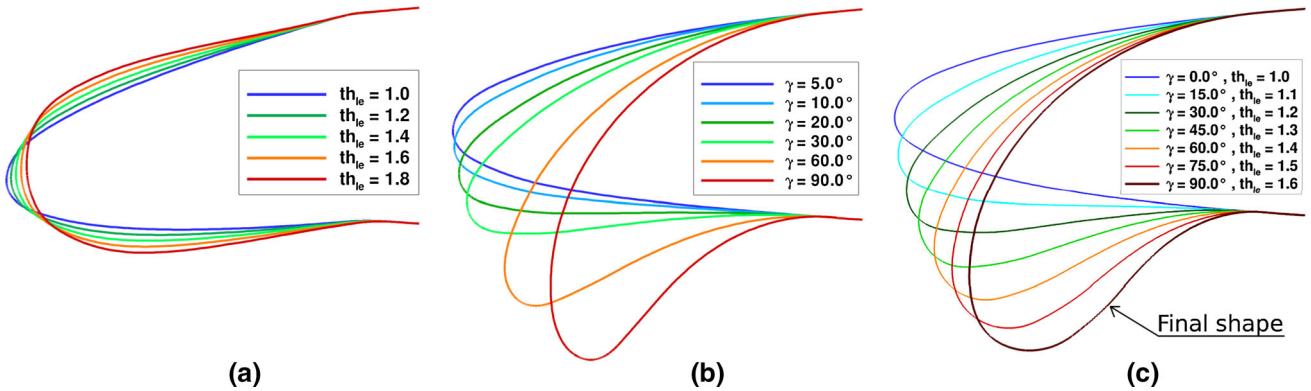

Fig. 16 Steps defining the flexible droop nose shape. **a** Thickness increase. **b** Smooth camber increase. **c** Smooth camber + thickness increase

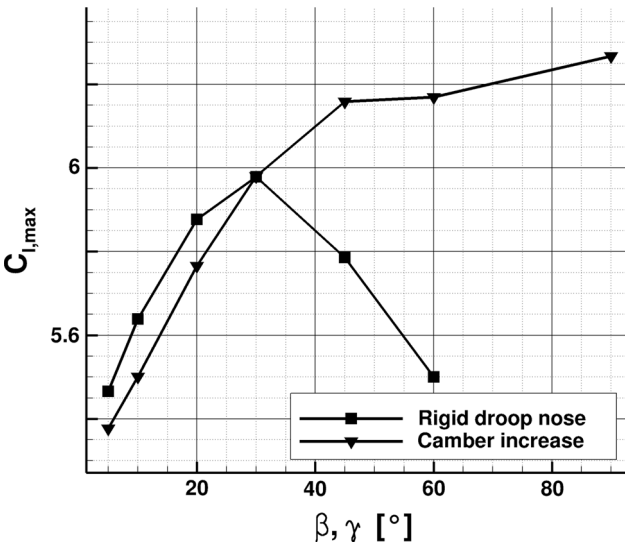

Fig. 17 Effects of camber increase on maximum lift, comparison between rigid nose rotation and smooth camber increase, $Re = 2 \times 10^7$, $M = 0.15$, $C_\mu = 0.06$

the leading-edge over the suction side of the airfoil, causes a slow down of the jet and a possible separation from the wall. This last phenomenon is affected by the characteristics of the outer flow upstream of the slot. As shown in the following paragraphs, an increase of the boundary-layer momentum thickness in this area gradually separates the outer flow from the jet, which then gets closer to the flap surface.

Based on these considerations, the analysis of the flow dynamics over the flap should take into account three co-dependent factors:

- Jet momentum coefficient: The momentum coefficient of the jet affects both the Coanda effect and the mixing between the jet and the outer flow. In the following, it is explained how these two effects are balanced, in relation to the nose shape, the angle of attack, and C_μ.
- Leading-edge influence or wake: The characteristics of the flow that is mixed with the jet are fundamental to the efficiency of the active high-lift system. The flow upstream of the slot is the result of the leading-edge behavior, the angle of attack, and the jet momentum coefficient.
- Angle of attack: The angle of attack varies the location of the stagnation point by changing the circulation. This affects the flow at the leading-edge, and consequently over the blowing slot. This results in a different flow behavior over the flap.

The reaction of the flow field to C_μ and α variations is quantified in the following sections by means of boundary-layer velocity profiles and thicknesses, evaluated at two important locations: over the slot, and near the trailing-edge (Fig. 18b).

Figure 19a shows the boundary-layer momentum thickness just before the jet reaches the trailing-edge. An increase in jet momentum coefficient improves the Coanda effect. The higher C_μ keeps the jet closer to the wall, thereby reducing the boundary-layer momentum thickness at the trailing-edge. An increase in α generates higher positive pressure gradients over the suction side of the airfoil, which increase the boundary-layer momentum thickness upstream of the slot. As a result, a gradual detachment occurs between outer flow and jet, which allows the jet to flow closer to the wall. In the following, examples of this phenomenon are presented.

Figure 19b shows the boundary-layer momentum thickness upstream of the blowing slot. For all the geometries, the angle of attack shows a significant influence on increasing the momentum thickness. However, the boundary layer that develops over the flexible droop nose appears less sensitive to variations of jet momentum than the other configurations (see also Fig. 20). This reduced sensitivity plays a key role in the stall behavior of the four configurations, as discussed in Sect. 6.3.4. The incidence

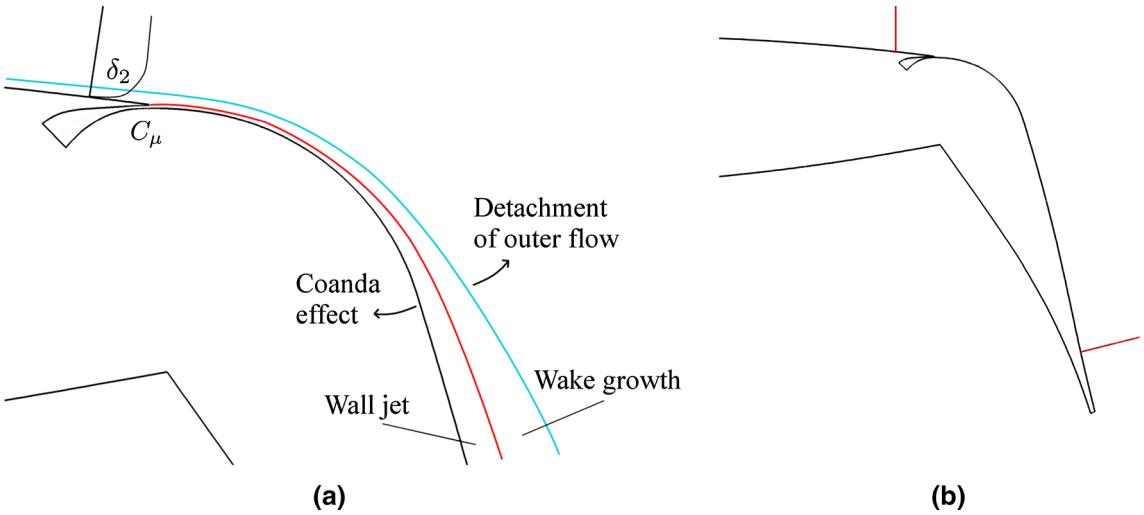

Fig. 18 References for the flow field analysis. **a** Working principle scheme of the Coanda flap. **b** Locations where the boundary layer is analyzed

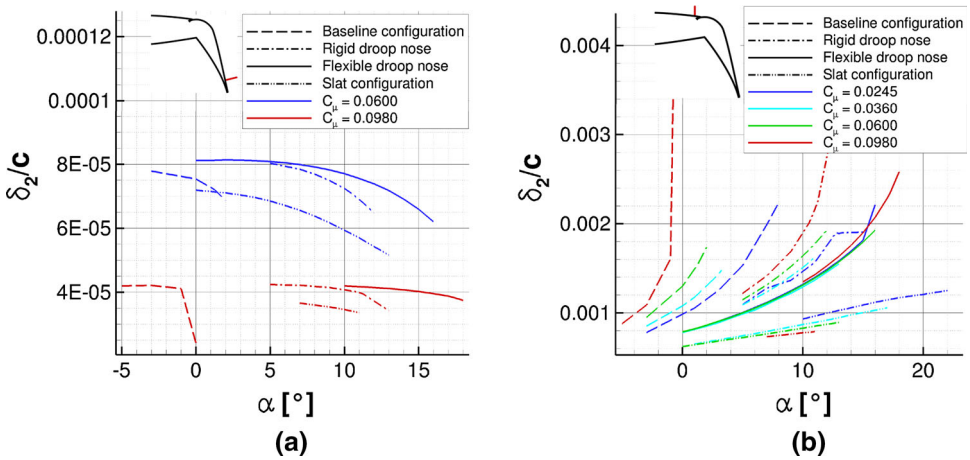

Fig. 19 Momentum thickness of the boundary layer at the two locations, for a range of C_μ and α, $Re = 12 \times 10^6$, $M = 0.15$. **a** Boundary-layer momentum thickness at the trailing-edge. **b** Boundary-layer momentum thickness over the slot

ranges, shown in Fig. 19b, include stall condition; however, no sudden growth of the momentum thickness is observed for most of the cases at high angles of attack. This confirms that stall is caused by a gradual reduction of the flow turning over the Coanda flap. Flow separation at the leading-edge occurs only for one particular case with high blowing and no leading-edge stall protection. On the other hand, the slat configuration shows an opposite trend in relation to the blowing momentum in comparison to the other leading-edge geometries, as higher C_μ results in lower boundary-layer momentum thickness. It is worthwhile to note that a higher C_μ causes a higher mass flow through the slat gap which results in a thinner boundary layer all over the suction side. On the other hand, the viscous losses on the slat surface, which create the slat wake (Fig. 20d at about h/c = 0.25), become more important for higher C_μ.

6 Results

6.1 Performance at constant blowing rate

In this section, a comparison among the different leading-edge configurations at constant blowing rate $C_\mu = 0.06$ is presented. This jet momentum coefficient ensures no separation from the flap even at stall condition. Stall is caused by a progressive decambering of the streamlines, which becomes more and more significant with increasing angle of attack. Details about the stalling mechanism are discussed in Sect. 6.3.4, whereas the present section focuses on the lift performance obtained by the different configurations. Figure 21a summarizes the shapes analyzed in the present work.

Figure 21b shows the effect the stall protection devices have on the lift performance. At this blowing rate, the

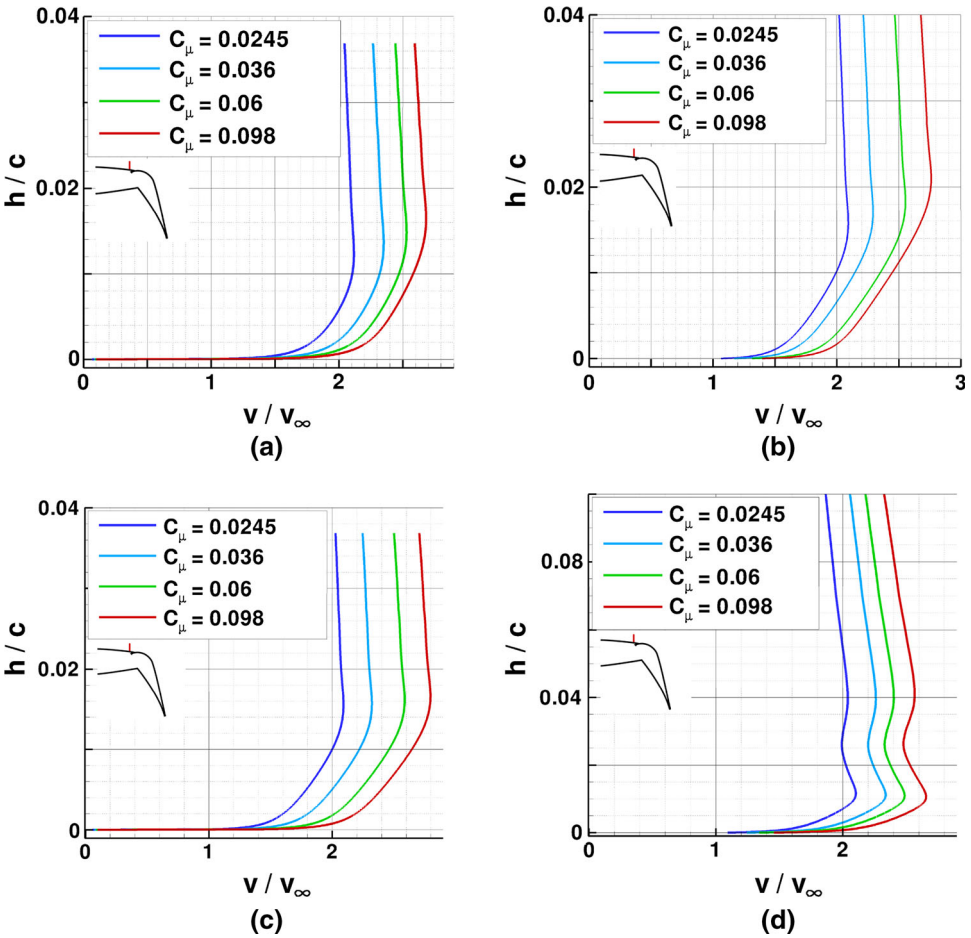

Fig. 20 Velocity profiles over the jet slot, at constant angles of attack, $Re = 12 \times 10^6$, $M = 0.15$. **a** Baseline, $\alpha = -3.0°$. **b** Rigid droop nose, $\alpha = 10.0°$. **c** Flexible droop nose, $\alpha = 10.0°$. **d** Slat nose, $\alpha = 10.0°$

flexible droop nose is the most effective configuration yielding the highest lift coefficient and stall angle, as reported in Table 3. The maximum lift benefit appears to be caused by the delayed stall angle, as the lift at low flow incidence is comparable. Figure 21c presents the pressure coefficient distributions at stall conditions for the four configurations. Note that the pressure at the Coanda surface is also affected by the leading-edge configuration, even for a constant jet momentum coefficient. The improved pressure distribution of the flexible droop nose is also apparent in Fig. 21d, where the C_p distributions are compared at the same angle of attack. The suction peak at the leading-edge is reduced by all the stall protection devices. However, the smooth camber line and thickness increase towards the nose, as described in Subsect. 5.1.2, distribute the low-pressure area over a larger surface, significantly reducing both the suction peak and the adverse pressure gradient. This distribution enables the flexible droop nose to reach higher stall angles. The aerodynamic coefficients resulting from the C_p distribution of Fig. 21d are reported in Table 4. In the incidence range of linear behavior, all configurations result in comparable lift for the same angle of attack.

A comparison between Fig. 21c, and Fig. 21d reveals that by increasing α the low pressure is transferred from the Coanda surface to the leading-edge. The decambering of the streamlines progressively unloads the flap, whereas increasing circulation accelerates the flow around the leading-edge.

The velocity profiles reported in Fig. 22 yield some physical insight into the flow dynamics generated by each leading-edge configuration. For all the cases, the increase of circulation due to a rising flow incidence results in higher edge velocities. However, in the absence of a stall protection device, the boundary-layer thickness is more sensitive to variations of angle of attack. This effect is significantly reduced by the two droop nose configurations. In particular, the high edge velocity of the flexible droop nose shows the extension of the low-pressure area over a large portion of the airfoil, yielding a reduced adverse pressure gradient. Figure 22d displays the different working principle of the slat configuration. The boundary layer on the main wing does not show a significant thickness variation with higher angles of attack. However, the momentum loss due to the wake of the slat becomes more important at high angles of attack. Moreover, with increasing α, the trace of the slat wake moves away from the airfoil wall. This means that the

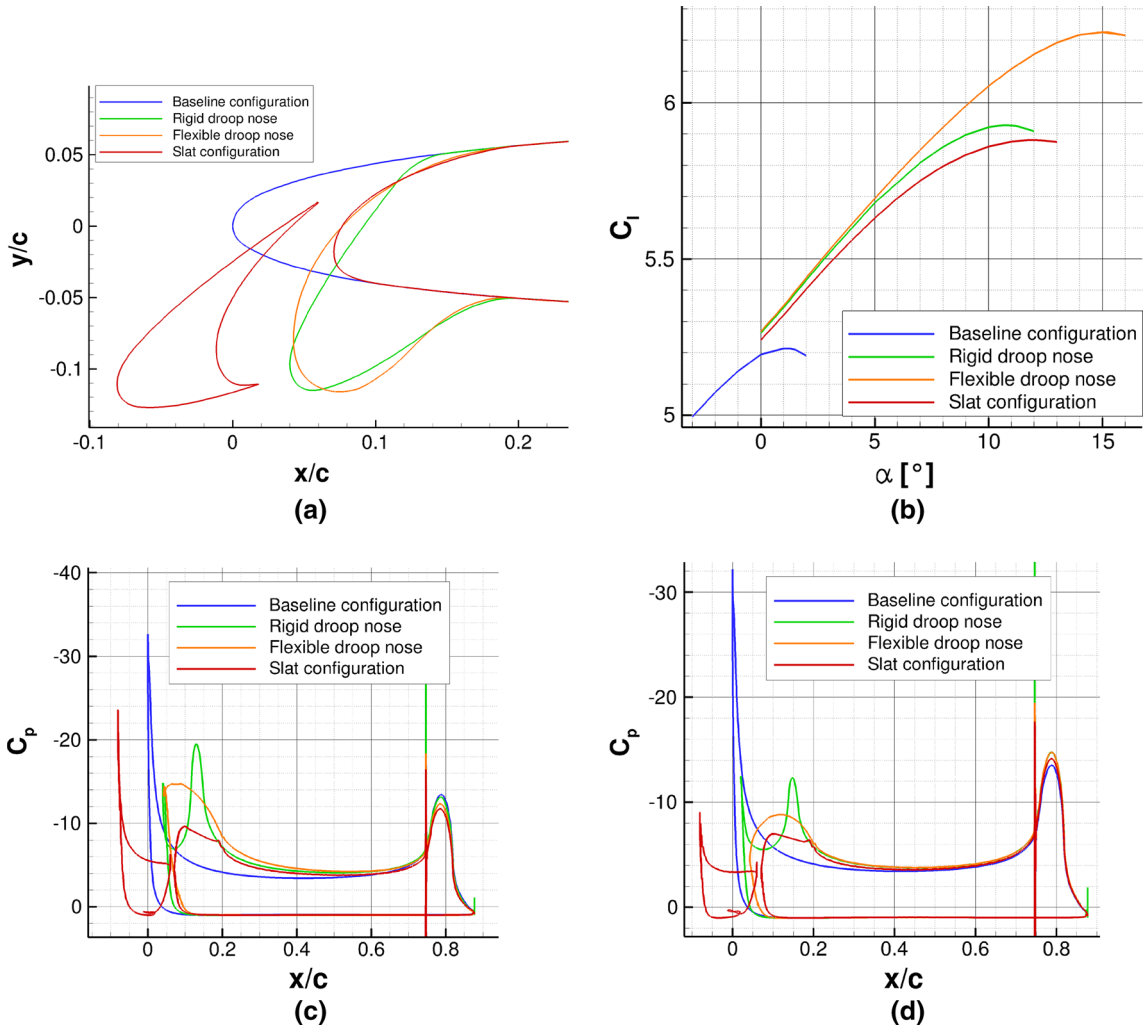

Fig. 21 Comparison among the tested leading-edge configurations at constant blowing rate, $C_\mu = 0.06$, $Re = 12 \times 10^6$, $M = 0.15$. **a** Shapes analyzed in the present work. **b** C_l comparison among the tested configurations. **c** C_p distributions at stall conditions. **d** C_p distributions at $\alpha = 1°$

Table 3 Maximum lift performances for $C_\mu = 0.06$, $Re = 12 \times 10^6$, $M = 0.15$

	$C_{l,max}$	α_{stall} (°)	$C_{d,stall}$	$C_{m,stall}$
Baseline configuration	5.214	1.25	0.07944	−0.9322
Rigid droop nose	5.928	10.75	0.09675	−0.9265
Flexible droop nose	6.226	15.0	0.11029	−0.8974
Slat configuration	5.880	12.0	0.11470	−0.6855

Table 4 Aerodynamic coefficient at $\alpha = 1°$, $C_\mu = 0.06$, $Re = 12 \times 10^6$, $M = 0.15$

	C_l	α (°)	C_d	C_m
Baseline configuration	5.214	1.0	0.07813	−0.9387
Rigid droop nose	5.345	1.0	0.06605	−1.0626
Flexible droop nose	5.351	1.0	0.06833	−1.0842
Slat configuration	5.321	1.0	0.07469	−0.9376

decambering of the streamlines due to boundary layer wakes subjected to adverse pressure gradient will occur differently for all four leading-edge configurations.

6.2 Effects of C_μ at constant angle of attack

The circulation is now varied by changing the blowing momentum, and the different leading-edge devices are compared at constant angle of attack, $\alpha = 10°$. Much lower angles of attack are not suitable for the three configurations with leading-edge device, as the flow on the airfoil lower surface may separate. For the baseline configuration, however, stall occurs at lower angles of attack. Therefore, this configuration is not included in the present analysis.

Figure 23a shows the effect of different blowing rates on the lift coefficient. For $C_\mu < 0.035$, the slat configuration yields the highest lift, whereas for higher blowing momentum coefficients the two droop nose approaches are

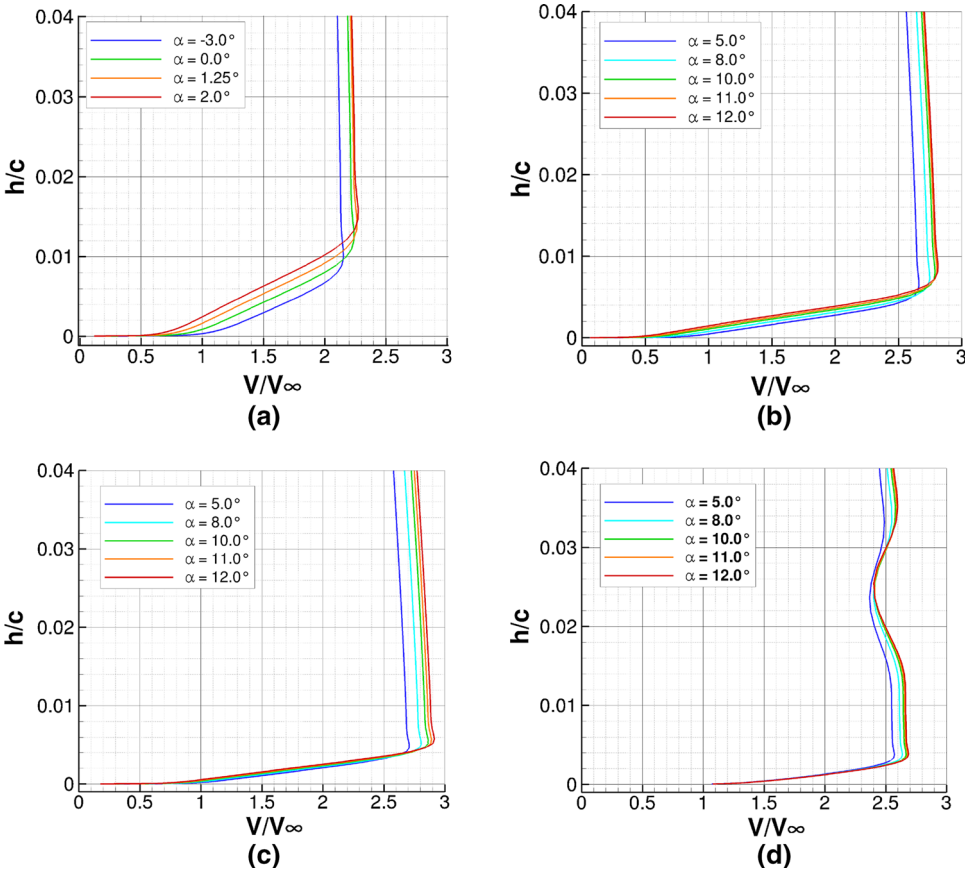

Fig. 22 Velocity profiles at 22 % of the airfoil chord, suction side, $Re = 12 \times 10^6$, $M = 0.15$, $C_\mu = 0.06$. **a** Baseline. **b** Rigid droop nose. **c** Flexible droop nose. **d** Slat configuration

more effective. The lift generated by the two droop nose configurations appears to be very similar over the entire range of C_μ. This means that the higher maximum lift yielded by the flexible droop nose is due to its increased stall angle of attack.

The drag coefficients, Fig. 23b, display the effect of the large separation over the flap for the cases of no or little blowing. $C_\mu = 0.0245$ already significantly reduces the pressure drag, even though an area of recirculation still exists over about 50 % of the flap. This separation disappears at $C_\mu = 0.0356$. However, the drag increase due to the higher lift is larger, resulting in a higher total drag. This effect seems to linearly increase the drag coefficient with the blowing rate, for all the configurations. The slat configuration presents a higher drag for all values of C_μ, because of the complex flow generated by the slat, e. g. the recirculation area in the concavity of the slat, the wake of the slat and its interaction with the main-wing boundary layer.

Increasing the blowing rate enhances flow turning over the flap, reducing pressure on the flap surface. This increases the negative pitching moment, as shown in Fig. 23c. The moment reference point is fixed for all the geometries at 25 % of the baseline chord. As seen in Table 3, the slat configuration yields the lowest moment, in absolute value. In addition, for the slat configuration at high C_μ, stall on pitching moment is observed. Stall is caused by a gradual decambering of the stream lines, which unloads the flap and reduces the negative pitching moment.

The behavior of the different leading-edge devices to blowing rate variations is described by displaying the velocity profiles at 22 % of the airfoil chord on the suction side in Fig. 24. The flexible droop nose yields the highest edge velocity, and the boundary-layer thickness appears to increase only slightly with the jet momentum. The boundary-layer thickness over the rigid droop nose shows a higher sensitivity to blowing rate variations. On the other hand, the boundary-layer thickness for the slat configuration is reduced with higher blowing rates. This is caused by the higher mass flow through the gap, due to the increased circulation. However, the wake of the slat becomes more important, showing increasing momentum losses. Similarly to the increase of circulation due to the angle of attack, described in the previous section, the distance of the slat wake from the wall increases.

6.3 Maximum lift performance

In this section, the performance of the four leading-edge configurations, in terms of maximum lift, is analyzed for

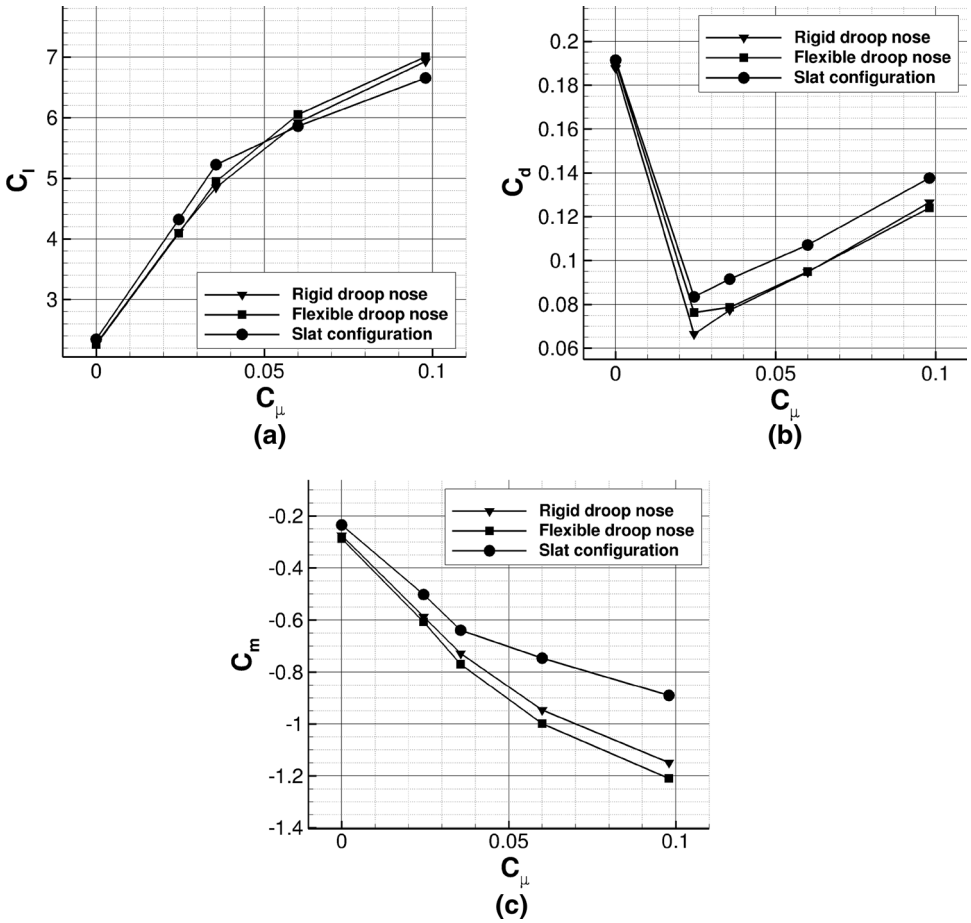

Fig. 23 Aerodynamic responses of the leading-edge devices to different blowing rates, at fixed angle of attack $\alpha = 10°$, $M = 0.15$, $Re = 12 \times 10^6$. **a** Lift coefficient. **b** Drag coefficient. **c** Pitching moment coefficient (25 % **c**)

different blowing rates. Note that the values corresponding to the no-blowing conditions are considered less accurate than the other cases, because of the large separation area that exists downstream of the 65° deflected flap. These regions are characterized by unsteady phenomena and vortices, which cannot be accurately captured with a RANS simulation. These separated cases typically present the lift fluctuations mentioned in Sect. 3.

6.3.1 *Effect of C_μ on maximum lift coefficient*

The addition of jet momentum involves an increase in circulation, which results in higher maximum lift, Fig. 25a. However, the efficiency of blowing decreases at high C_μ. For low momentum, the graph has a higher slope, and describes the regime of boundary-layer control. Here, C_μ is not sufficient to keep the flow attached until the trailing-edge, causing the jet to separate from the wall. The separation point can be delayed by increasing C_μ, until the trailing-edge is reached. At this point, a second regime begins, which is referred to as the supercirculation regime. The increase of C_l after this point is achieved by a further deflection of the streamlines due to the jet effect downstream of the trailing-edge. This explains the lower efficiency of this second region: in order to obtain the same improvement of C_l, a higher increase of blowing power is needed.

6.3.2 *Effect of C_μ on stall angle of attack*

The stall angle of attack directly depends on the interaction between the flow dynamics at the leading-edge and at the flap. As mentioned above, the trailing-edge device increases the suction at the leading-edge, which deteriorates the overall airfoil performance. This can be improved by different means of leading-edge stall protection that create different stall mechanisms. This explains the different trends shown in Fig. 25b. As the $C_{l,\,max}$, the stall angle of attack is sensitive to the different regimes: boundary-layer control and supercirculation. A more detailed discussion about the various stalling behaviors is presented in the next sections.

6.3.3 *Optimal blowing rate*

The border between boundary-layer control and supercirculation regimes represents the optimal blowing rate, since it yields the highest lift gain without loss of efficiency. A

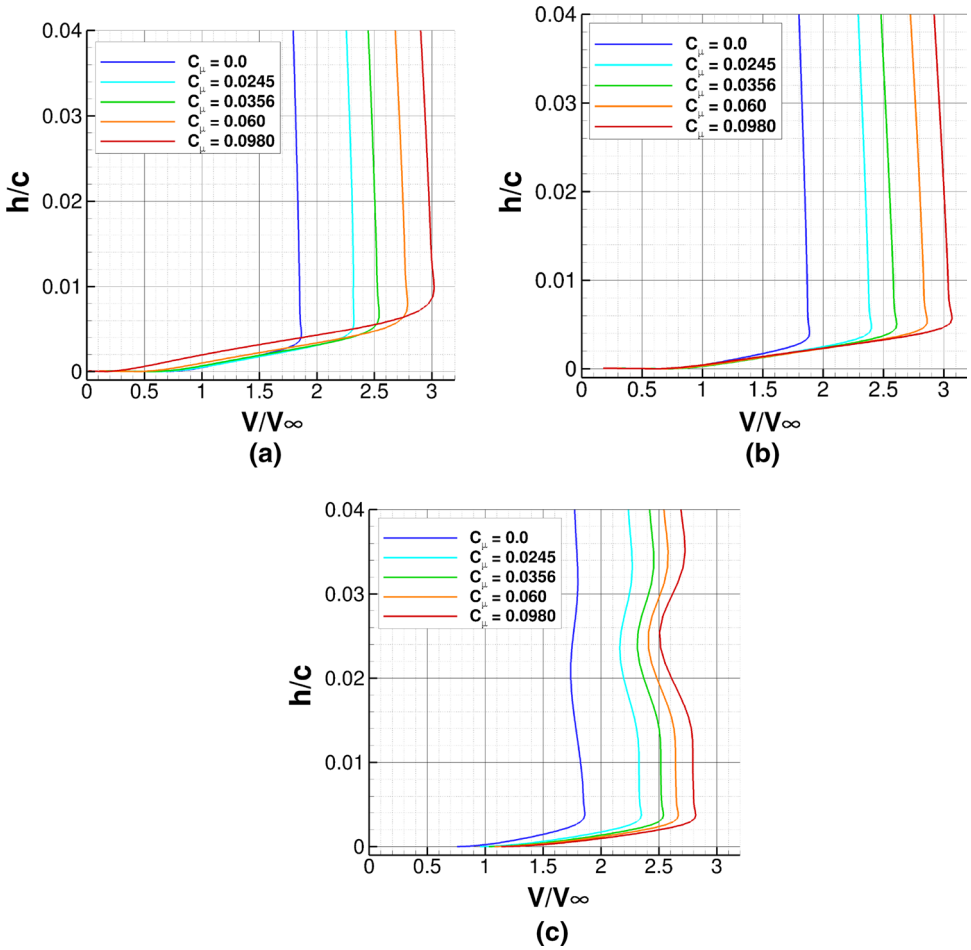

Fig. 24 Velocity profiles at 22 % of profile chord for different blowing rates, at fixed angle of attack $\alpha = 10°$, $M = 0.15$, $Re = 12 \times 10^6$. **a** Rigid droop nose. **b** Flexible droop nose. **c** Slat configuration

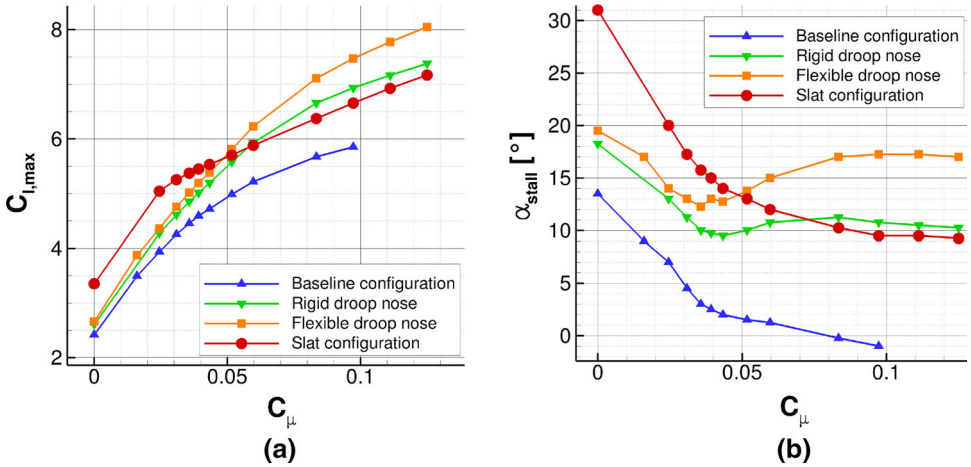

Fig. 25 Response of the four airfoils to different momentum coefficients, $M = 0.15$, $Re = 12 \times 10^6$. **a** Effect of C_μ on the maximum lift coefficient. **b** Effect of C_μ on the stall angle of attack

lower blowing rate would provide more flow turning with a lower flap deflection, which would lead to attached flow. In the same way, a higher blowing rate could be employed with a higher flap angle. This observation defines a natural correspondence between jet momentum and flap deflection angle. However, in the present work the flap angle is kept constant for the entire C_μ range since the main purpose of the study is the analysis of the leading-edge device. Moreover, in order to analyze and understand the overall behavior of the high-lift configuration, it is worthwhile to also investigate the stalling mechanism for blowing rate values away from the optimum.

The transition between boundary-layer control and supercirculation regimes is more evident for baseline and slat configurations. While the nominal momentum coefficient of the Coanda flap is the value that ensures attached flow

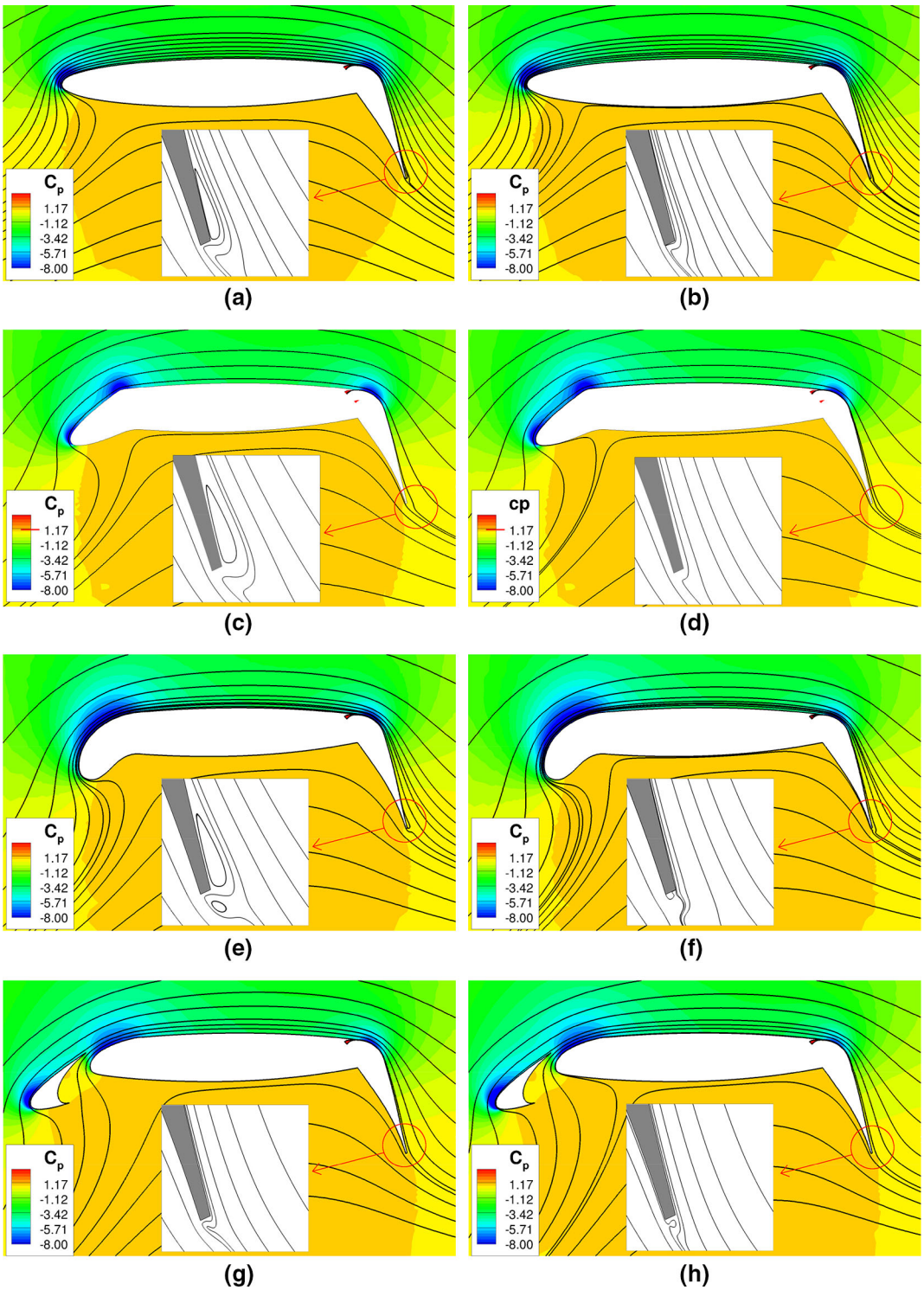

Fig. 26 Flow evolution near stall conditions at optimum blowing rate, $C_\mu = 0.0356$, $M = 0.15$, $Re = 12 \times 10^6$. **a** Baseline, $\alpha = 1.0°$, $C_l = 4.413$. **b** Baseline, $\alpha_{stall} = 3.0°$, $C_{l,max} = 4.456$. **c** Rigid droop nose, $\alpha = 8°$, $C_l = 4.805$. **d** Rigid droop nose, $\alpha_{stall} = 10°$, $C_{l,max} = 4.851$. **e** Flexible droop nose, $\alpha = 10.0°$, $C_l = 4.948$. **f** Flexible droop nose, $\alpha_{stall} = 12.25°$, $C_{l,max} = 5.018$. **g** Slat configuration, $\alpha = 14.0°$, $C_l = 5.362$. **h** Slat configuration, $\alpha_{stall} = 16.0°$, $C_{l,max} = 5.372$

until the trailing-edge, this condition is also affected by the angle of attack. Figure 26 shows the evolution of the flow field for angles of attack close to stall. For all the configurations the nominal momentum coefficient is around 0.036. A small separation occurs at the trailing-edge for the baseline and the two droop nose configurations

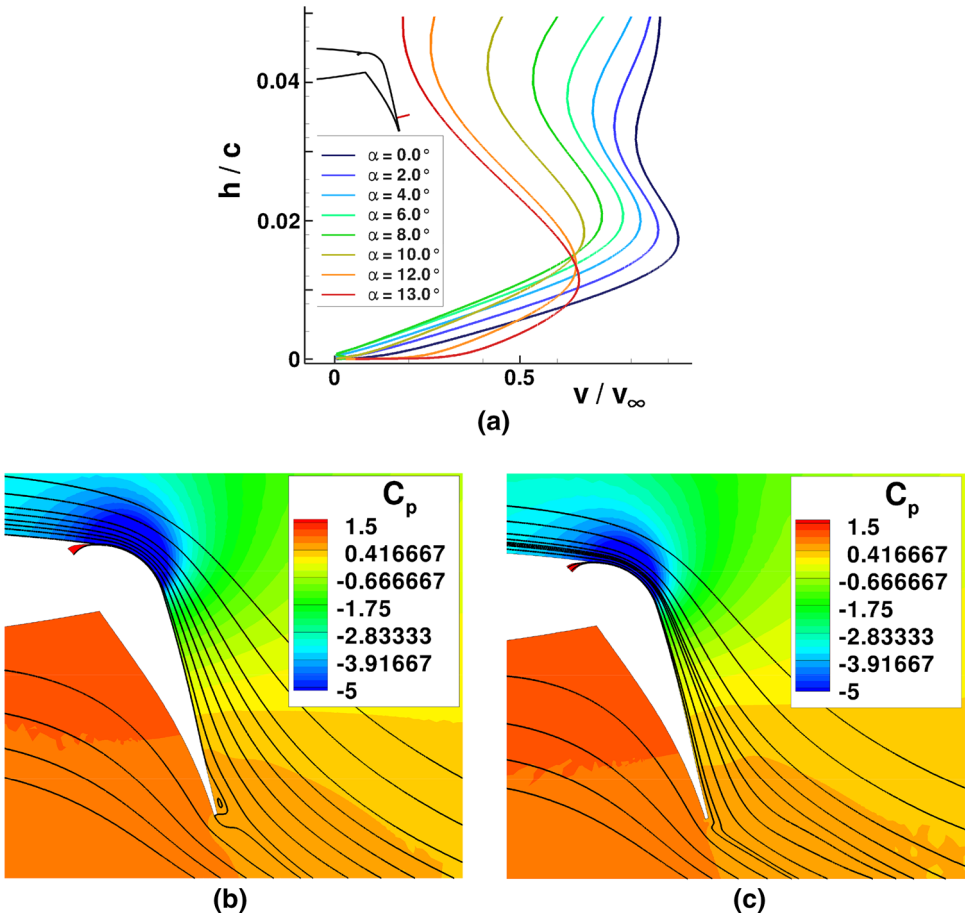

Fig. 27 Flow features and trailing-edge boundary-layer evolution for $C_\mu = 0.0356$, flexible droop nose, $M = 0.15$, $Re = 12 \times 10^6$. **a** Velocity profiles at 0.05 chord ahead of the trailing-edge. **b** $\alpha = 8.0°$. **c** $\alpha = 13.0°$

until a few degrees before stall. At stall conditions the flow is completely attached, as discussed in the next section.

6.3.4 Stall mechanisms

The phenomena that generate stall appear to be strongly affected by the leading-edge device. The following paragraphs describe the evolution of the flow at high angles of attack, and explain the trends shown in Fig. 25. Figures 28, 29, 30, and 31 show some flow fields describing the stall conditions for the four configurations. The pictures are organized in tables, where the three rows correspond to different jet momentum coefficients: 0.0245, 0.06 and 0.098. The central picture of every row displays the flow at maximum lift, whereas the first column shows the flow a few degrees before stall and the third one represents stalled conditions.

In boundary-layer control regime the jet does not have sufficient momentum to keep the outer flow attached to the flap surface until the trailing-edge. The first row of the result Figs. 28, 29, 30, and 31 illustrate this condition, for $C_\mu = 0.0245$. At low angles of attack the jet separates from the wall following the same path as the outer flow. As the angle of attack increases, the positive pressure gradient over the flap and over the main part of the airfoil increases. Figure 27 illustrates the behavior of the wall jet upstream of the separation point for the flexible droop nose configuration at $C_\mu = 0.0356$. Until $\alpha = 8.0°$ the positive pressure gradient decreases the slope of the velocity close to the wall. On the other hand, for higher angles of attack the increased suction at the leading-edge, which increases the boundary-layer momentum thickness over the slot, becomes more important. As a consequence, the attachment between the jet and the outer flow decreases, and the jet flow is closer to the flap surface. This phenomenon can cause the separation to disappear, even without leading-edge separation, as one can see in Fig. 27b, c. In some cases, a recirculation area occurs between the jet and the outer flow. This happens typically for low blowing rates, as shown in Figs. 28b, c, 29b, c and 31c. Note that, the very high losses at the leading-edge caused by high C_μ in the baseline configuration can cause a similar flow topology, Fig. 28i.

An increase in C_μ improves both the Coanda effect and the momentum transferred to the outer flow. As a result, the separation point is moved toward the trailing-edge. This increases the lift coefficient but decreases the stall angle of attack. Indeed, since the separation occurs closer to the trailing-edge, the local positive pressure gradient is more

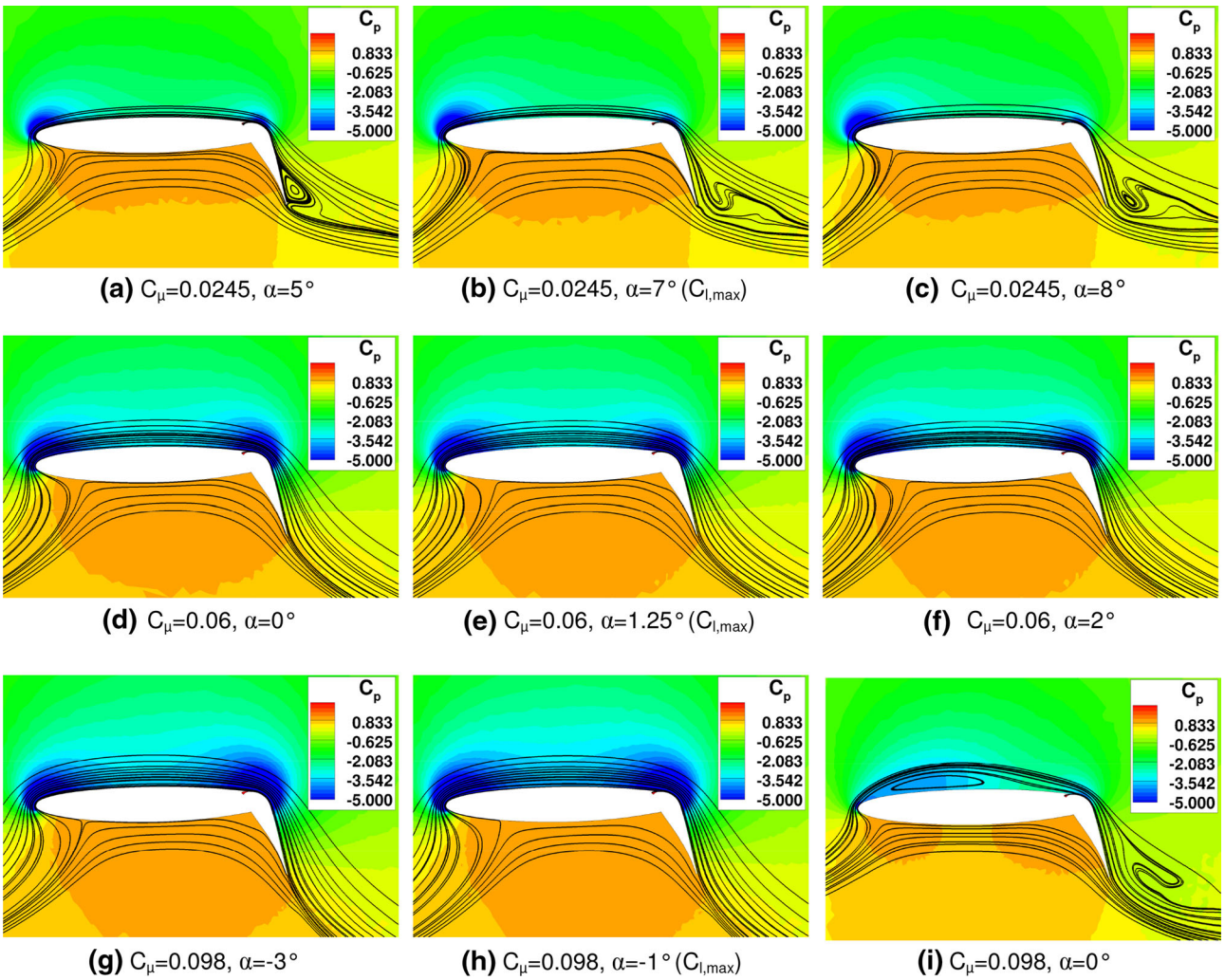

Fig. 28 Baseline configuration: C_p contour and streamlines, $M = 0.15$, $Re = 12 \times 10^6$. **a** $C_\mu = 0.0245$, $\alpha = 5°$. **b** $C_\mu = 0.0245$, $\alpha = 7°$ ($C_{l,max}$). **c** $C_\mu = 0.0245$, $\alpha = 8°$. **d** $C_\mu = 0.06$, $\alpha = 0°$. **e** $C_\mu = 0.06$, $\alpha = 1.25°$ ($C_{l,max}$). **f** $C_\mu = 0.06$, $\alpha = 2°$. **g** $C_\mu = 0.098$, $\alpha = 3°$. **h** $C_\mu = 0.098$, $\alpha = -1°$ ($C_{l,max}$). **i** $C_\mu = 0.098$, $\alpha = 0°$

sensitive to α. Therefore, the progressive separation between the jet and the outer flow begins at lower angles of attack.

In supercirculation regime, the jet has sufficient momentum to always stay attached to the flap surface. Therefore, the jet trajectory remains mostly constant, contrarily to the previous case. In this regime, the leading-edge configuration plays a more important role, as it affects the momentum losses of the outer flow upstream of the slot. As mentioned above, the momentum of the outer flow has an important influence on the mixing between jet and outer flow. For all the configurations, higher C_μ corresponds to more momentum transferred to the outer flow from the jet. For the baseline configuration, higher C_μ significantly increases the boundary-layer momentum thickness over the slot, whereas with the slat configuration the momentum losses occur in the wake of the slat, see Fig. 20d. Here, the growth of the wake losses with C_μ leads to the reduction of the stall angle with increased blowing rate, as observed in Fig. 25b. For the droop nose geometries, the effect of an increased jet momentum coefficient on the momentum losses of the outer flow is less important (Fig. 20b). Therefore, the outer flow will overcome higher positive pressure gradients, and stall is delayed. This behavior is sustained until $C_\mu \sim 0.08$.

6.4 Overall lift gains

As mentioned in the introduction, a suitable parameter to evaluate the efficiency of the active high-lift system is the ratio between the increase of lift coefficient yielded by the active flow control and the momentum coefficient needed to obtain that gain:

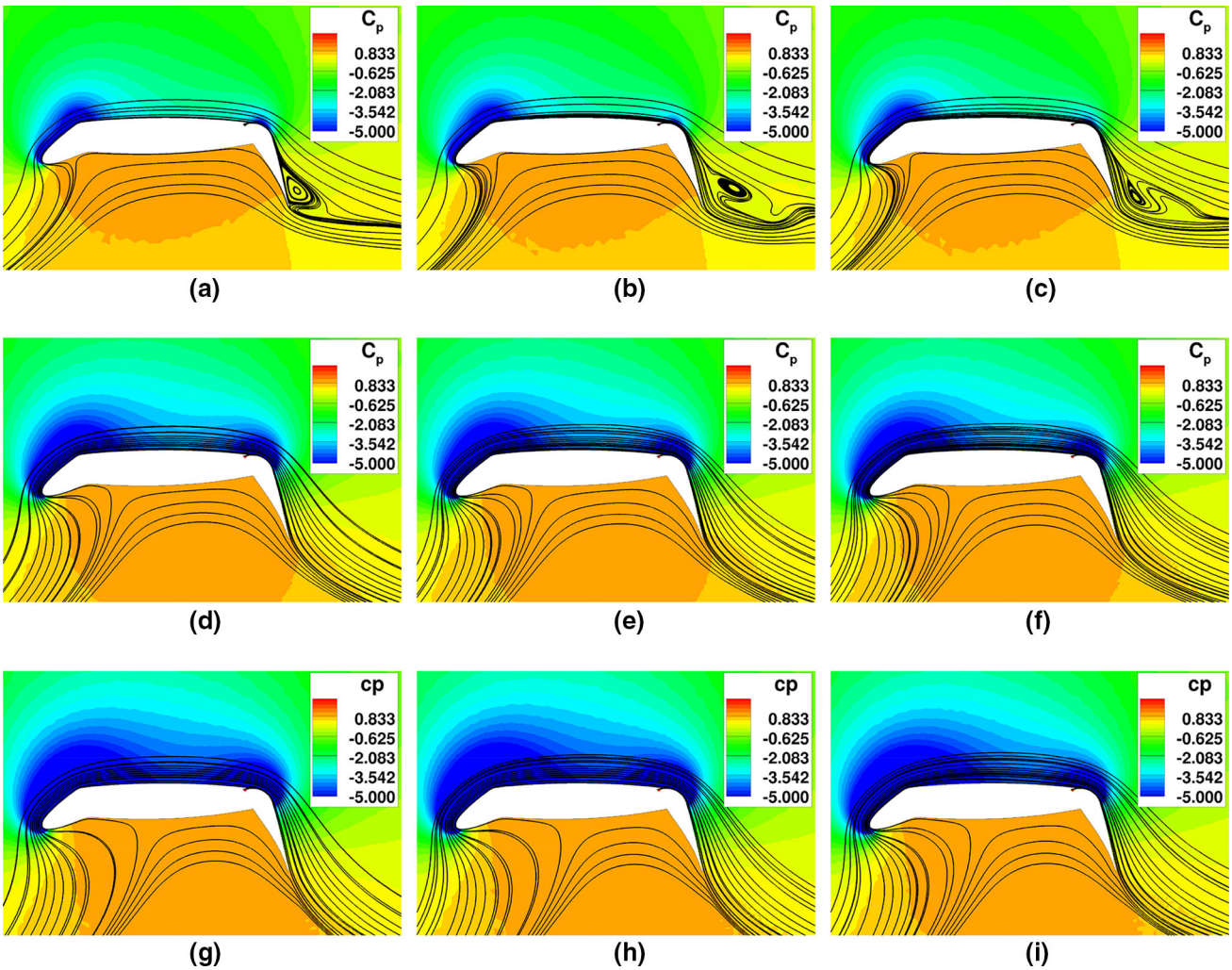

Fig. 29 Rigid droop nose configuration: C_p contour and streamlines, $M = 0.15$, $Re = 12 \times 10^6$. **a** $C_\mu = 0.0245$, $\alpha = 11°$. **b** $C_\mu = 0.0245$, $\alpha = 13°$ ($C_{l,max}$). **c** $C_\mu = 0.0245$, $\alpha = 15°$. **d** $C_\mu = 0.06$, $\alpha = 9°$. **e** $C_\mu = 0.06$, $\alpha = 10.75°$ ($C_{l,max}$). **f** $C_\mu = 0.06$, $\alpha = 12°$. **g** $C_\mu = 0.098$, $\alpha = 9°$. **h** $CC = 0.098$, $\alpha = 10.75°$ ($C_{l,max}$). **i** $C_\mu = 0.098$, $\alpha = 13°$

$$\text{Lift Gain Factor (LGF)} = \frac{C_{l_{\text{max, blowing}}} - C_{l_{\text{max, reference}}}}{C_\mu}.$$

Figure 32 shows the evolution of the LGF with C_μ. The figure displays two different approaches to compute the lift gain factor. In Fig. 32a, the reference $C_{l,max}$ is the lift coefficient obtained by each leading-edge configuration without blowing. This comparison allows us to evaluate the efficiency of the Coanda flap when combined with the different leading-edge shapes. The increase of lift produced by blowing with the flexible droop nose appears to be the highest, whereas the slat configuration needs more blowing in order to obtain a certain increase of maximum lift. This is due to the already high lift coefficient produced by the slat configuration with no blowing. As mentioned above, the stall angle of attack and the lift coefficient obtained for moderate blowing rate by the slat configuration are significantly higher than for the other cases. In Fig. 32b, the LGF refers to maximum lift obtained by the airfoil in cruise configuration, without flap and leading-edge device. Hence, one obtains the overall improvement of the high-lift system with respect to its cruise configuration. Here the slat leading-edge generates the highest benefit, for C_μ lower than 0.05. Above this value the flexible droop nose is more effective.

Another estimate of the gains yielded by the stall protection devices is obtained by examining the blowing rate needed to generate a target lift. Note that certain lift coefficients may be generated by different combinations of blowing rate, flap angle, and angle of attack. As we aim at indentifying the minimum blowing rate that provides a target C_l, we simply chose the angle of maximum lift. Using the present computational data base for this estimate we can obtain approximate results in the following sense:

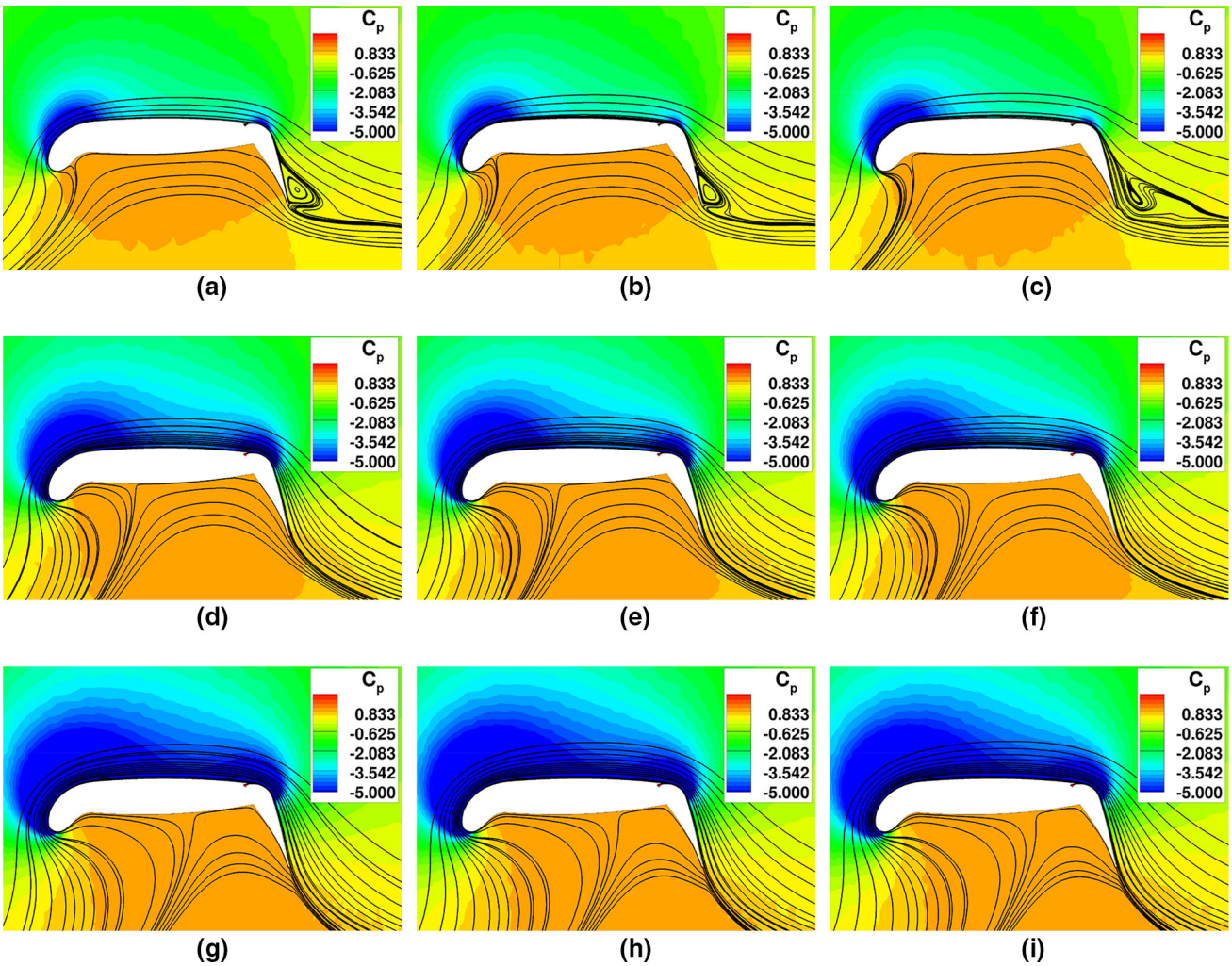

Fig. 30 Flexible droop nose configuration: C_p contour and streamlines, $M = 0.15$, $Re = 12 \times 10^6$. **a** $C_\mu = 0.0245$, $\alpha = 12°$. **b** $C_\mu = 0.0245$, $\alpha = 14°$ ($C_{l,max}$). **c** $C_\mu = 0.0245$, $\alpha = 15°$. **d** $C_\mu = 0.06$, $\alpha = 13°$. **e** $C_\mu = 0.06$, $\alpha = 15°$ ($C_{l,max}$). **f** $C_\mu = 0.06$, $\alpha = 16°$. **g** $C_\mu = 0.098$, $\alpha = 15°$. **h** $C_\mu = 0.098$, $\alpha = 17°$ ($C_{l,max}$). **i** $C_\mu = 0.098$, $\alpha = 18°$

- The flap deflection angle is not varied. Therefore, the results are fairly accurate only around $C_\mu \approx 0.0356$ which is the optimal blowing rate for all investigated leading-edge configurations, according to Sect. 6.3.3.
- Only a discrete number of blowing rates have been employed so far. Therefore, a linear interpolation was performed to obtain the data for a given target lift coefficient.

Even if not rigorously accurate the present analysis can point out the expected benefits of the different leading-edge configurations in possible aircraft applications. A target lift coefficient of $C_{l,max} = 5.0$ was chosen, which yielded the interpolated results summarized in Table 5.

As can be seen in the table, all leading-edge devices reduce the required momentum coefficient of blowing by significant amounts. The slat configuration requires the lowest values, followed by the flexible droop nose. Again, the pitching moment around the reference point 25 % c is also given. The absolute value of the pitching moment is now significantly lower in the case of flexible droop nose, compared to the baseline configuration, as the distribution of leading-edge suction is better distributed. However, with respect to the same reference point, the slat configuration offers the best improvement of pitching moment, due to the high load on the slat and the extended chord.

7 Conclusion

New results on the combination of well-designed Coanda flaps and leading-edge stall protection devices are presented. This combination brings a large increase in

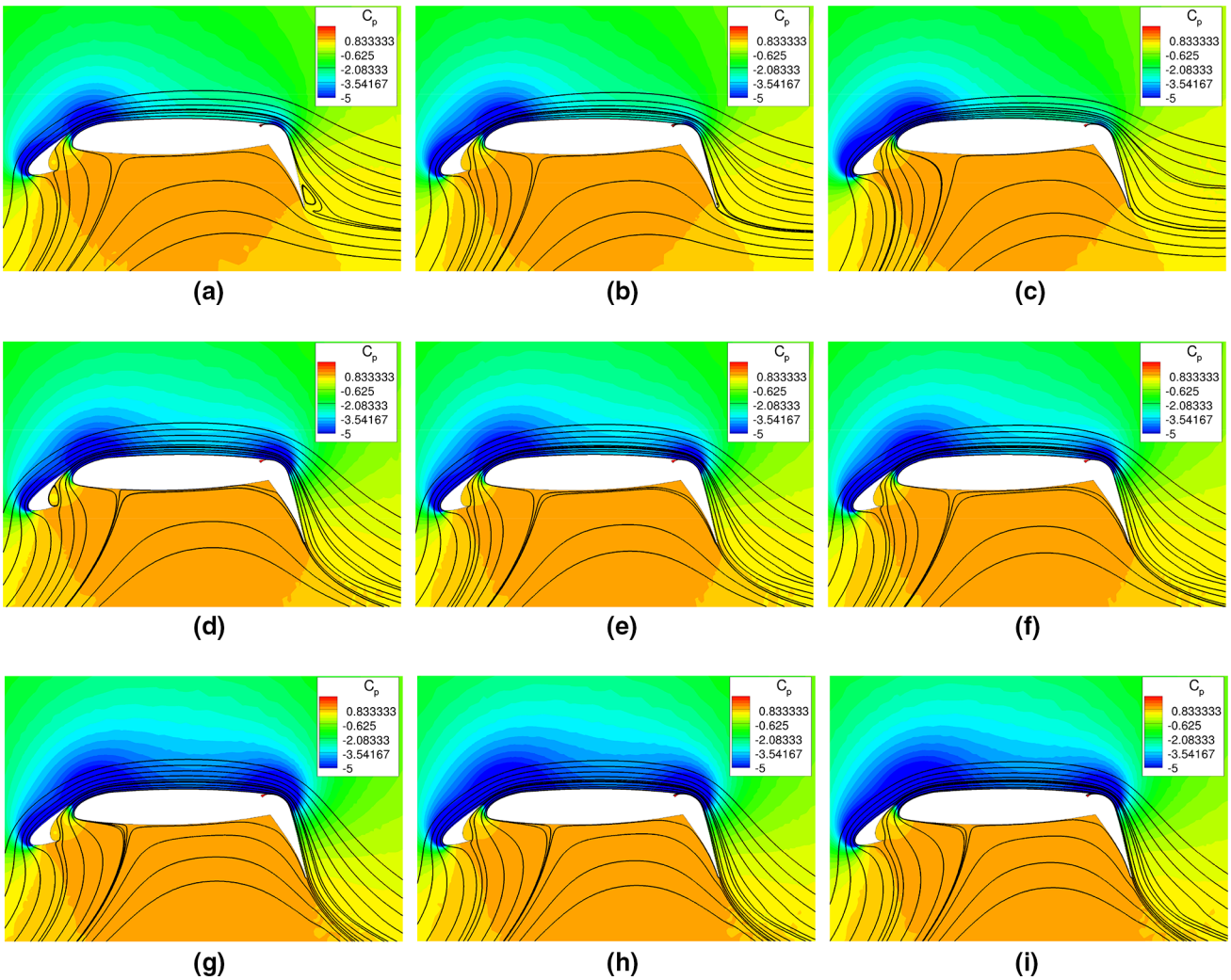

Fig. 31 Slat configuration: C_p contour and streamlines, $M = 0.15$, $Re = 12 \times 10^6$. **a** $C_\mu = 0.0245$, $\alpha = 18°$. **b** $C_\mu = 0.0245$, $\alpha = 20°$ ($C_{l,max}$). **c** $C_\mu = 0.0245$, $\alpha = 22°$. **d** $C_\mu = 0.06$, $\alpha = 10°$. **e** $C_\mu = 0.06$, $\alpha = 12°$ ($C_{l,max}$). **f** $C_\mu = 0.06$, $\alpha = 13°$. **g** $C_\mu = 0.098$, $\alpha = 7°$. **h** $C_\mu = 0.098$, $\alpha = 9.5°$ ($C_{l,max}$). *i* $C_\mu = 0.098$, $\alpha = 11°$

maximum lift coefficient and stall angle of attack with respect to the configuration without leading-edge device. In particular, for C_μ higher than 0.036, these improvements appear to be larger than for the combination of a flexible droop nose with a conventional Fowler flap device. The improvements in maximum lift can be used to reduce the blowing rate needed to reach a target lift. For example, a target maximum lift coefficient of 5 can be obtained with about 32 % less jet momentum with the flexible droop nose, which improves the lift gain factor by the same proportion. This benefit is increased to 56 % by the slat configuration for momentum coefficients below about 0.05, but at the likely increase of airframe noise due to the gap flow with high velocities at the slat trailing-edge. Moreover, the stall angle of attack in this lift range is brought to values suitable for landing and take-off operations: from 1.5° to 12.3° for the flexible droop nose and to 20.6° for the slat configuration. The pitching moment represents an important issue for the stability of the aircraft, and due to an improved load distribution along the chord and the lower jet momentum requirement, the pitching moment is improved by 18 % thanks to the flexible droop nose and by 65 % with the slat configuration. Another result of the present analysis is the quantification of the benefits yielded by a flexible droop nose with respect to a conventional rigid leading-edge flap: the target lift coefficient of 5.0 can be achieved with 9 % less blowing momentum, and the stall angle is increased by 2.3°. These improvements increase with the blowing rate.

The analysis of stall mechanisms highlighted some important, unexpected phenomena:

– Progressive attachment of the wall jet to the flap for an increasing angle of attack.

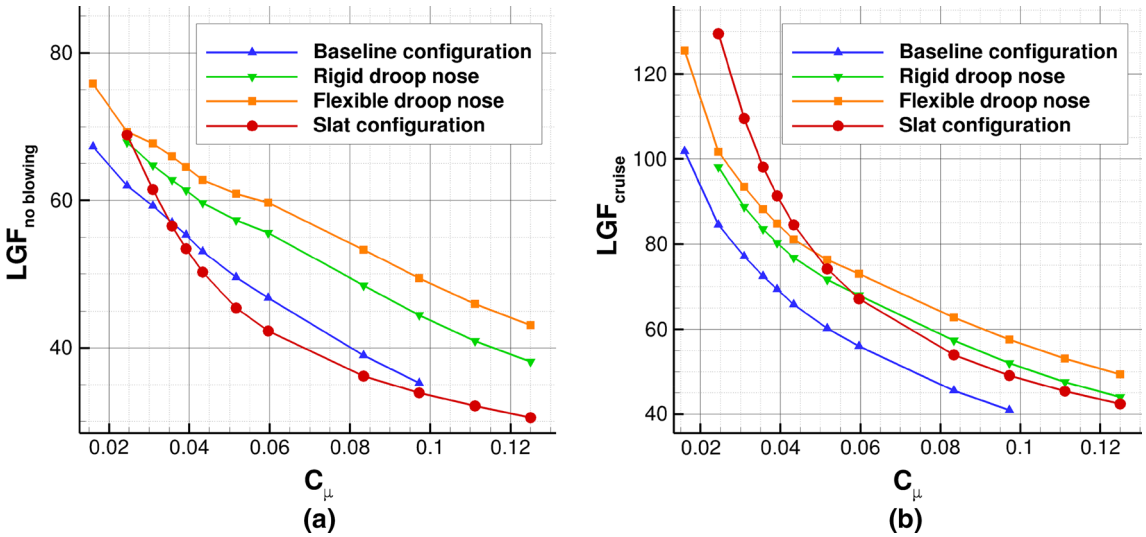

Fig. 32 Effects of blowing rates on lift gain factor, $M = 0.15$, $Re = 12 \times 10^6$. **a** LGF for the various cases, with no-blowing cases as reference. **b** LGF for the various cases, with cruise configuration lift coefficient used as reference

Table 5 Aerodynamic coefficients at same maximum lift, $M = 0.15$, $Re = 12 \times 10^6$

	C_μ	α_{stall} (°)	$C_{l,\ max}$	$C_{m,\ stall}$
Baseline configuration	0.0522	1.5	5.0	−0.880
Rigid droop nose	0.0389	10.0	5.0	−0.764
Flexible droop nose	0.0353	12.3	5.0	−0.724
Slat configuration	0.0232	20.6	5.0	−0.304

- Separation between the wall jet and the outer flow in the case of low blowing rates, which creates a complex recirculation area between the two flow streams.
- The droop nose yields increased stall angles of attack for large wall jet momentum coefficients.

The flow analysis also led to a more thorough understanding of the boundary-layer development upstream of the slot and on the flap, which depends on the angle of attack and blowing rate. This knowledge will play an important role in the design of an open- and close-loop control for the blowing device, which is planned for the future development of the high-lift system. Pulsed blowing may interact with the flow structures mentioned above, increasing the blowing system efficiency. Moreover, pressure and skin friction sensors could be strategically positioned over the airfoil surface at critical flow areas, and their signals would be used to efficiently control the jet. The blowing rate would be adapted to the actual flow condition, leading to an overall reduction of the required blowing power.

We note that the presented flow simulations will have to be confirmed by the use of more advanced turbulence models, as well as by experimental results. Water tunnel experiments are planned at the Technische Universität Braunschweig, where the droop nose geometry analyzed in the present paper will be employed.

Acknowledgments The funding of this work of the Collaborative Research Centre SFB 880 by the German Research Foundation, DFG, is thankfully acknowledged.

References

1. Wild, J.: Mach and Reynolds number dependencies of the stall behavior of high-lift wing-sections. J. Aircr. **50**(4), 1202–1216 (2013)
2. Radespiel, R., Heinze, W.: SFB 880: Fundamentals of High-Lift for Future Commercial Aircraft. Deutscher Luft- und Raumfahrtkongress, Stuttgart (2013)
3. Werner-Spatz, C., Heinze, W., Horst, P., Radespiel, R.: Multidisciplinary conceptual design for aircraft with circulation control high-lift systems. CEAS Aeronaut. J. **3**, 145–164 (2012)
4. Pott-Pollenske, M., Alvarez-Gonzalez, J., Dobrzynski, W.: Effect of slat gap on farfield radiated noise and correlation with local flow characteristic. 9th AIAA/CEAS Aeroacoustics Conference, Hilton Head (SC), AIAA 2003-3228
5. Nielsen, J.N., Biggers, J.C.: Recent progress in circulation control aerodynamics, AIAA Paper 87-001, (1987)
6. Greenblatt, D., Wygnanski, I.: The control of flow separation by periodic excitation. PERGAMON Prog. Aerosp. Sci. **36**, 487–545 (2000)
7. Yaros, S.F., et al.: Synergistic Airframe-Propulsion Interactions and Integrations, NASA/TM-1998-207644, (1998)
8. Joslin, R.D., Jones, G.S.: Applications of Circulation Control Technology. Progress in Astronautics and Aeronautics, vol. 214, AIAA, (2006)
9. Gad El Hak: Flow Control: Passive, Active, and Reactive Flow Management. Cambridge University Press, England (2000)
10. Englar, R.J.: Overview of circulation control pneumatic aerodynamics: blown force and moment augmentation and modification

as applied primarily to fixed-wing aircraft. In: Joslin, D., Jones, G.S. (eds.) Applications of Circulation Control Technology, Progress in Astronautics and Aeronautics, vol. 214, pp. 23–68, AIAA, (2006)
11. Milholen, W., Jones, G., Chan, D.: High-Reynolds number circulation control testing in the national transonic facility (Invited). 50th AIAA Aerospace Sciences Meeting, AIAA 2012-0103
12. Allan, B., Jones, G., Lin, J.: Reynolds-Averaged Navier-Stokes simulation of a 2D circulation control wind tunnel experiment, 49th AIAA Aerospace Sciences Meeting, Orlando (FL), AIAA 2011-25
13. Paschal, K., Neuhart, D., Beeler, G., Allan, B.: Circulation Control Model Experimental Database for CFD Validation, 50th AIAA Aerospace Sciences Meeting, Nashville (TN), AIAA 2012-0705
14. Pott-Pollenske, M., Pfingsten, K.-C.: Aeroacoustic Performance of an Airfoil with Coanda Control, 16th AIAA/CEAS Aeroacoustics Conference, AIAA 2010-3881, (2010)
15. Schwier, W.: Auftriebsanderung Durch einen auf der Flugeldruckseite Ausgeblasene Luftstrahl, UM31912, (1944)
16. Poisson-Quinton, Ph, Lepage, L.: Survey of French research on the control of boundary layer and circulation. In: Lachmann, G.V. (ed.) Boundary Layer and Flow Control: its Principles and Application, vol. 1, pp. 21–73. Pergamon, New York (1961)
17. Radespiel, R., Pfingsten, K.-C., Jensch, C.: Flow analysis of augmented high-lift systems, In: Radespiel, R., Rossow, C.-C., Brinkmann, B. (eds.) Hermann Schlichting—100 Years. Scientific Colloquium Celebrating the Anniversary of his Birthday, Braunschweig, Germany 2007. Notes on Numerical Fluid Mechanics and Multidisciplinary Design, vol. 102, Springer, ISBN978-3-540-95997-7, (2009)
18. Thomas, F.: Untersuchungen über die Grenzschichtbeeinflussung durch Ausblasen zur Erhöhung des Auftriebes, Dissertation, Institut für Strömungsmechanik, TU Braunschweig, 1961. Gekürzte Fassung: Z. Flugwiss. vol. 10, pp. 46–65, (1962)
19. Gersten, K., Löhr, R.: Untersuchungen über die Auftriebserhöhung eines Tragflügels bei gleichzeitigem Ausblasen an der Hinterkantenklappe und an der Profilnase, Institutsbericht 62/34, Institut für Strömungsmechanik der Technischen Universität Braunschweig, (1962)
20. Englar, R.J., Huson, G.G.: Development of advanced circulation control using high-lift airfoils. J. Aircr. **21**(7), 476–483 (1984)
21. Jensch, C., Pfingsten, K.C., Radespiel, R., Schuermann, M., Haupt, M., Bauss, S.: Design Aspects of a Gapless High-Lift System with Active Blowing. DLRK 2009, Aachen (2009)
22. Englar, R.J., Smith, M.J., Kelley, S.M., Rover II, R.C.: Development of circulation control technology for application to advanced subsonic transport aircraft. J. Aircr. **31**(7), 1160–1177 (1994)
23. Greenblatt, D.: Dual Location Separation Control on a Semi-Span Wing, 23rd AIAA Applied Aerodynamics Conference, Toronto, Ontario Canada (2005)
24. Jensch, C., Pfingsten, K.C., Radespiel, R.: Numerical investigation of leading edge blowing and optimization of the slot and flap geometry for a circulation control airfoil. Notes on Numerical Fluid Mechanics and Multidisciplinary Design, vol. 112. Springer, Heidelberg (2010)
25. Seifert, A.: Delay of airfoil stall by periodic excitation. J Aircr, vol. 33, no. 4, July–August (1996)
26. Kühn, T., Wild, J.: Aerodynamic optimization of a two-dimensional two-element high lift airfoil with a smart droop nose device, 1st EASN Association Workshop on Aerostructures. Paris, France (2010)
27. Shmilovich, A., Yadlin, Y.: Flow control for the systematic buildup of high lift systems. 3rd AIAA Flow Control Conference, San Francisco (CA), AIAA 2006-2855
28. Shmilovich, A., Yadlin, Y.: Flow control techniques for transport aircraft. AIAA J. **49**, 489–502 (2011)
29. Ying, S.X., Spaid, F.W., McGinley, C.B., Rumsey, C.L.: Investigation of confluent boundary layers in high-lift flows, AIAA Paper 1998-2622, (1998)
30. Jirásek, A., Amoignon, O.: Design of a high-lift system with a droop nose device. J. Aircr. **46**, 731–734 (2009)
31. Burnazzi, M., Radespiel, R.: Design and analysis of a droop nose for coanda flap applications. J. Aircr. (2014). doi:10.2514/1.C032434
32. Pfingsten, K.C., Jensch, C., Körber, K.V., Radespiel, R.: Numerical simulation of the flow around circulation control airfoils. First CEAS European Air and Space Conference, Berlin (2007)
33. Swanson, R.C., Rumsey, C.L.: Computation of circulation control airfoil flows. Comput. Fluids **38**, 1925–1942 (2009)
34. Pfingsten, K.C., Cecora, R.D., Radespiel, R.: An experimental investigation of a gapless high-lift system using circulation control. Katenet II Conference, Bremen (2009)
35. Pfingsten, K.C., Radespiel, R.: Experimental and numerical investigation of a circulation control airfoil. 47th AIAA Aerospace Sciences Meeting, Orlando, AIAA 2009-533
36. Kroll, N., Rossow, C–.C., Schwamborn, D., Becker, K., Heller, G.: MEGAFLOW—A Numerical Flow Simulation Tool for Transport Aircraft Design. ICAS Congress, Toronto (2002)
37. Schamborn, D., Gerhold, T., Heinrich, R.: The DLR TAU-Code: Recent Applications in Research and Industry. ECCOMAS CFD, Egmond aan Zee (2006)
38. Shur, M.L., Strelets, M.K., Travin, A.K., Spalart, P.R.: Turbulence modeling in rotating and curved channels: assessing the spalart-shur correction. AIAA J. **38**, 784–792 (2000)
39. Richardson, L.F.: The deferred approach to the limit. Trans. Royal. Soc. Lond. Series A **226**, 299–361 (1927)
40. Raymer, D.P.: Aircraft design: a conceptual approach. AIAA Educ. Ser., (1999)